

University of Nebraska - Lincoln

DigitalCommons@University of Nebraska - Lincoln

Mechanical (and Materials) Engineering --
Dissertations, Theses, and Student Research

Mechanical & Materials Engineering,
Department of

Summer 8-2021

Thermomechanical Modeling in Laser Powder Bed Fusion Additive Manufacturing using Graph Theory: Application to Prediction of Recoater Crash

Md Humaun Kobir

University of Nebraska - Lincoln, mkobir2@huskers.unl.edu

Follow this and additional works at: <https://digitalcommons.unl.edu/mechengdiss>



Part of the [Applied Mechanics Commons](#)

Kobir, Md Humaun, "Thermomechanical Modeling in Laser Powder Bed Fusion Additive Manufacturing using Graph Theory: Application to Prediction of Recoater Crash" (2021). *Mechanical (and Materials) Engineering -- Dissertations, Theses, and Student Research*. 176.

<https://digitalcommons.unl.edu/mechengdiss/176>

This Article is brought to you for free and open access by the Mechanical & Materials Engineering, Department of at DigitalCommons@University of Nebraska - Lincoln. It has been accepted for inclusion in Mechanical (and Materials) Engineering -- Dissertations, Theses, and Student Research by an authorized administrator of DigitalCommons@University of Nebraska - Lincoln.

THERMOMECHANICAL MODELING IN LASER POWDER BED FUSION
ADDITIVE MANUFACTURING USING GRAPH THEORY: APPLICATION TO
PREDICTION OF RECOATER CRASH

by

Md Humaun Kobir

A THESIS

Presented to the Faculty of
The Graduate College at the University of Nebraska
In Partial Fulfillment of Requirements
For the Degree of Master of Science
Major: Mechanical Engineering & Applied Mechanics

Under the Supervision of Professor Prahalada Rao
Lincoln, Nebraska
August 2021

THERMOMECHANICAL MODELING IN LASER POWDER BED FUSION
ADDITIVE MANUFACTURING USING GRAPH THEORY: APPLICATION TO
PREDICTION OF RECOATER CRASH

Md Humaun Kobir, M.S.

University of Nebraska, 2021

Advisor: Prahalada Rao

This work pertains to the laser powder bed fusion (LPBF) additive manufacturing process. The objective of this thesis is to predict a frequently occurring type of thermal-induced process failure in LPBF called recoater crash. To ascertain the likelihood of a recoater crash before the part is printed, we develop and apply a computationally efficient thermomechanical modeling approach based on graph theory.

Despite its demonstrated ability to overcome the design and processing constraints of conventional subtractive and formative manufacturing, the production-level scaleup of LPBF is hindered by frequent build failures. For example, the part often deforms as it is being printed due to uneven heating and cooling. This thermal-induced deformation of the LPBF part during processing causes it to interfere with the deposition mechanism (recoater) leading to a common build failure called recoater crash. A recoater crash not only destroys the part involved but also causes an entire build to be abandoned resulting in considerable time and material losses.

In this context, fast and accurate thermomechanical simulations are valuable for practitioners to identify and correct problems in the part design and processing conditions that can lead to a recoater crash before the part is even printed. Herein, we propose a novel

thermomechanical modeling approach to predict recoater crashes which is based on two sequential steps. First, the temperature distribution of the part during printing is predicted using a meshfree graph theory-based computational thermal model. Second, the temperature distribution is used as an input into a finite element model to predict recoater crashes. The accuracy and computational efficiency of this graph theory-based approach is demonstrated in comparison with both non-proprietary thermomechanical finite element analysis (Abaqus), and a proprietary LPBF simulation software (Netfabb). Based on numerical (verification) and experimental (validation) studies, the proposed approach is 5 to 6 times faster than the non-proprietary finite element modeling and has the same order of speed as Netfabb. This physics-based approach to prevent recoater crashes can engender substantial savings by supplanting existing build-and-test optimizations of part design and parameters.

Acknowledgements

I would like to express my sincere gratitude to my thesis advisor Dr. Prahalada Rao for his consistent support and patience throughout my graduate school. His guidance and motivation have been instrumental in the completion of this work. I appreciate you always helping me in every step of this academic mission. I would also like to thank the thesis committee members, Dr. Kevin Cole and Dr. Carl Nelson, for their valuable advice, insight, and recommendations to improve the quality of this work.

I would like to acknowledge the help and support of my colleagues in the completion of this hard outcome. This thesis would not have been accomplished without the help, support, and guidance provided by Dr. Reza Yavari.

I would also like to thank the National Science Foundation (NSF) for funding this work through grant no. CMMI 1752069.

Finally, I would like to thank my family for their undying support and love. Thank you, Husna, for always understanding me. I especially want to thank my parents for their continuous support and guidance throughout my entire life.

Table of Contents

Chapter 1 – Introduction	1
1.1 Motivation and Background	1
1.2 Objective, Hypothesis, and Scope	5
1.3 Literature Review.....	6
Chapter 2 – Approach	14
2.1 Overview of Thermal Modeling in AM using Graph Theory.....	16
2.2 Thermomechanical Analysis using Graph Theory and Finite Element Modeling	20
Chapter 3 – Verification with Finite Element Method	29
3.1 Procedure	29
3.2 Test Parts.....	31
3.3 Model Calibration and Convergence	33
3.4 C-shaped Part without Supports.....	37
3.4.1 Thermal History Prediction	37
3.4.2 Deformation Prediction	39
3.5 C-shaped Part with Supports.....	42
3.5.1 Thermal History Prediction	42
3.5.2 Deformation Prediction	44
Chapter 4 – Experimental Validation	47
4.1 Prediction of Thermal History	51
4.2 Prediction of Recoater Crash	54
Chapter 5 – Conclusions and Future Work.....	59
References Cited	61

List of Figures

Figure 1: A schematic of the laser powder bed fusion (LPBF) process. Image from Yavari <i>et al.</i> [6].	1
Figure 2: (Top) The build plate used for the experimental validation in this work, note the failed arch-shaped parts and damage to the lattice-like N-shaped part. (Bottom) The superelevation of the arches and N-shaped part leads to a subsequent recoater crash.	3
Figure 3: Available thermomechanical modeling approaches to predict thermal-induced deformation are categorized based on the computational technique.	13
Figure 4: The sequential steps of graph theory-based thermomechanical modeling wherein the graph theory thermal model uses the input parameters to estimate thermal history. Next, the FE-based mechanical model receives the thermal history from the graph theory model and computes thermal-induced deformation.	14
Figure 5: Schematic representation of graph theory approach in the context of the LPBF process. The key to the process is to determine the thermal history of the part using graph theory thermal modeling. This information is then transferred to finite element analysis to determine thermal-induced deformation.	19
Figure 6: (a) C-shaped part without supports, (b) C-shaped part with supports.	32
Figure 7: LPBF knee implant with thin supports showing over the heated surface at the overhang region. Image from Yavari <i>et al.</i> [6].	32
Figure 8: Calibration of (a) graph theory thermal model for node density as the number of nodes per mm^3 and (b) coupled thermomechanical FE model for mesh element size in mm. In the graph theory thermal model, increasing the node density results in better convergence while in coupled thermomechanical FE model, reducing the element size improves the prediction accuracy. In this work, we selected the node density $5.0 \text{ nodes} \cdot \text{mm}^{-3}$ and mesh element size 0.5 mm. The asterisk* represents the origin ($x = 0, y = 0, z = 0$) of the C-shaped parts.	36

Figure 9: Thermal history of the C-shaped part without supports. (a) Average surface temperature measured at the end of the layer. (b) & (c) Surface temperature at a specific location (4, 1, z) mm and (7, 1, z) mm,. The red line in the figure represents the thermal history predicted using the graph theory approach with ± 1 standard deviation over 10 replications, whereas the black line is the thermal history predicted using the coupled thermomechanical FE model which is considered as the ground truth. 38

Figure 10: Qualitative comparison of thermal history predictions at the completion of the part from (a) coupled thermomechanical FE model, (b) graph theory (Thermal) model, and (c) Netfabb. 39

Figure 11: Comparison of predicted deformation of C-shaped part without supports between the coupled thermomechanical FE model and the graph theory-based approach showing (a) maximum deformation of each layer, (b) average layer deformation, and (c) & (d) deformation measured at (4, 1, z) mm, and (7, 1, z) mm, respectively, along the build direction. 40

Figure 12: Thermal history of the C-shaped part with supports showing (a) average surface temperature at the end of each layer; (b) & (c) are the temperatures measured at two different coordinates for different layer heights of z (4 mm, 1 mm, z mm), and (17 mm, 1 mm, z mm), respectively..... 43

Figure 13: Qualitative comparison of the thermal history predictions at the completion of the part from (a) coupled thermomechanical FE model, (b) graph theory (Thermal) model, and (c) Netfabb. 43

Figure 14: Comparison of deformation predictions for C-shaped part with supports between the coupled thermomechanical FE and the graph theory (Deformation) approaches..... 45

Figure 15: The schematic of the open architecture build platform and photograph of the setup. A longwave infrared thermal camera located above the build plate and inclined at 80° to the horizontal plane is used to capture the part surface temperature during the build process. Image from Yavari *et al.* [90]. 48

Figure 16: Arch-Shaped geometries (with/without supports) with varying gauge thicknesses, $t = 0.5, 1.0, 1.5, 2.0,$ and 2.5 mm..... 49

Figure 17: IR camera images of recoater crash incidents at layers 548, 556, and 574 corresponding to arches A10, A05, and A25 & A20. Note that the relative intensity of the failed arches is higher compared to the other arches which indicate relatively higher heat retention occurring following the recoater interference with these arches. The debris of the crashed arch A10 is still evident in the subsequent layers. Image from Yavari *et al.* [90].
.....50

Figure 18: The surface temperature observed during experiments (blue line) overlaid on the coupled thermomechanical FE model (black), and graph theory (red) thermal history predictions for four representative arches (a) A10, (b) A20, (c) A25, and (d) SA25. 52

Figure 19: Qualitative comparison of the thermal history predictions for arches 2.5 mm with (SA25) and without (A25) supports at the completion of three different build heights from coupled thermomechanical FE model, graph theory (Thermal), and Netfabb..... 53

Figure 20: Deformation predictions of each layer using coupled thermomechanical FE (black), graph theory-based (red), and Netfabb (green) models corresponding to the arches (a) A10, (b) A20, (c) A25, and (d) SA25. The recoater crash occurs when deformation exceeds the layer height of 40 μm (red dotted). 55

Figure 21: Qualitative comparison of the deformation predictions at three different build heights using coupled thermomechanical FE, graph theory (Deformation), and Netfabb models of the arch without supports A25 and arch with supports SA25..... 56

CHAPTER 1 – INTRODUCTION

1.1 Motivation and Background

In the laser powder bed fusion (LPBF) metal additive manufacturing process, thin layers of powder are deposited and selectively melted using energy from a laser to form a three-dimensional part [1]. A schematic of the LPBF process is shown in Figure 1. The process can revolutionize functional performance in strategic applications ranging from aerospace to biomedical industries [2-4]. For instance, using LPBF to make an aircraft engine decreased the number of parts from 855 to 12 and increased fuel efficiency as well as engine power by 20 percent [5].

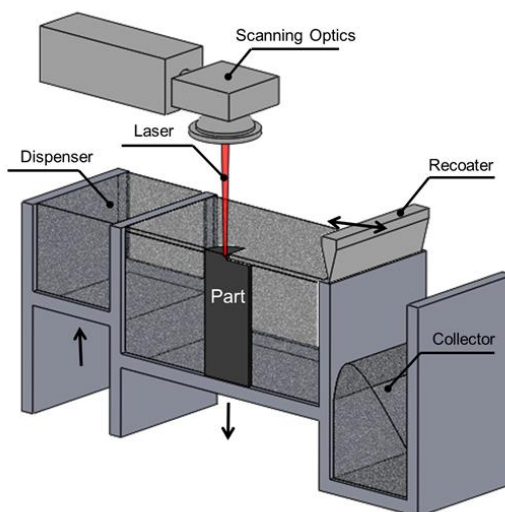


Figure 1: A schematic of the laser powder bed fusion (LPBF) process. Image from Yavari *et al.* [6].

However, poor process consistency and degraded part quality currently afflict LPBF, and print failure rates often exceed 30 percent due to a lack of responsive process control [7-11]. Thus, precision-oriented industries are reluctant to use LPBF to make safety-critical

parts [9-15]. Hence, to ensure broader use of LPBF parts, potential causes of flaw formation must be understood, predicted, and mitigated.

Flaw formation in LPBF parts is influenced by the spatiotemporal temperature distribution – thermal history – as they are being printed [10]. To make an LPBF part, a laser melts individual tracks of material at scanning speeds close to 1,000 mm per second. Consequently, the heating and cooling cycles often exceed 10^5 degrees Celsius per second [16, 17]. The thermal history is a complex function of the part shape, material properties, and 50+ processing parameters [18-20]. Therefore, parameters optimized by empirical testing of simple-shaped coupons may not work for complex parts [11, 21].

A particular type of frequently occurring build failure called recoater crash – the focus of this work – is directly related to the thermal history. Due to the uneven heating and cooling of the part during printing, the part deforms, and its top surface extends (raises) above the thin layer of powder. This phenomenon is called superelevation. If the deformation of the top surface of the part in the vertical build direction is larger than the layer height (typically 20 to 50 μm), the part will interfere with the recoater as it attempts to deposit a new layer of powder. The resulting contact of the part with the recoater may damage the part; fine features are particularly vulnerable for failure due to recoater crash. Furthermore, following a crash the recoater drags debris from the failed part across the build plate. This debris from the recoater crash can potentially damage other parts of the build plate. Often an entire build must be discarded due to a recoater crash.

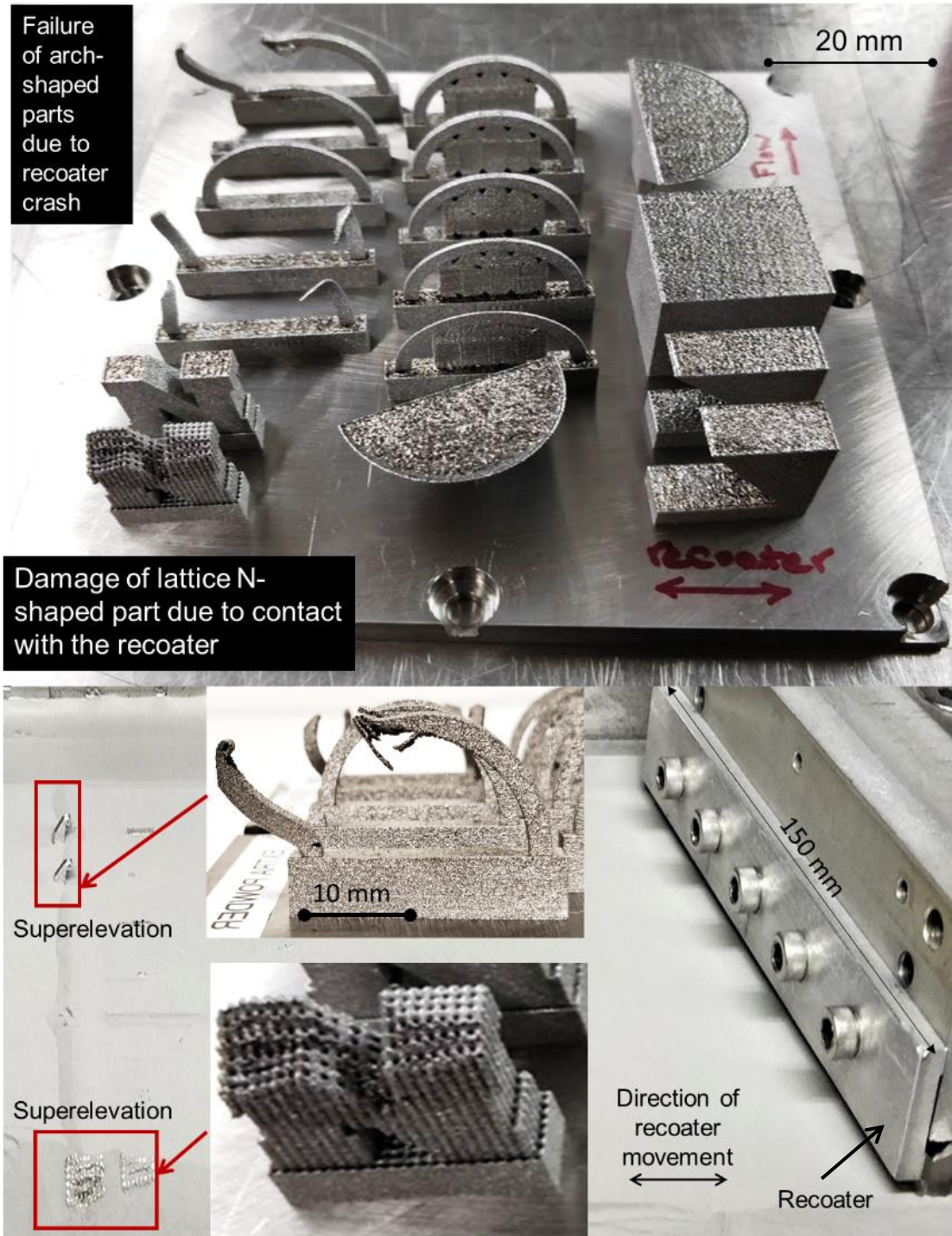


Figure 2: (Top) The build plate used for the experimental validation in this work, note the failed arch-shaped parts and damage to the lattice-like N-shaped part. (Bottom) The superelevation of the arches and N-shaped part leads to a subsequent recoater crash.

Examples of recoater crashes are exemplified in Figure 2. Shown in Figure 2 (top) is an LPBF build plate consisting of several Inconel 718 parts of different shapes. All these parts were built under identical processing conditions. Near the left edge of the build plate are five arch-shaped parts built without supports. A similar failure of features is observed for the N-shaped part with a lattice-like structure owing to superelevation and subsequent contact with the recoater. In Figure 2 (bottom), the occurrence of superelevation of the arch and N-shaped parts is evident.

In Figure 2 (top), it is observed that the arch-shaped parts built with support structures did not fail, unlike their counterparts without supports. The arches without supports tend to retain heat, leading to the uneven temperature distribution. Supports, by providing a conduit to rapidly conduct the heat, avoid heat retention, thus, avoiding superelevation. The foregoing example further illustrates the causal interaction of part design and quality in LPBF.

Currently, practitioners resort to an empirical build-and-test approach to optimize the part geometry, placement of supports, part orientation, and process parameters to avoid recoater crashes – an expensive and time-consuming process. Moreover, such empirical optimization efforts are tightly linked to the build plan because the addition or removal of parts from the build plate changes the thermal history. Thus, in the context of Figure 2, fast and accurate thermal simulations that can replace trial-and-error experiments are critical for reducing build failures and facilitating production-level scaling of LPBF parts.

1.2 Objective, Hypothesis, and Scope

The objective of this work is to predict the thermal-induced deformation in LPBF parts as they are being printed, and consequently, forecast the occurrence of recoater crashes using a graph theory-based thermomechanical modeling approach.

The approach is based on two sequential steps. First, the thermal history of the part is predicted using a meshfree graph theory-based computation thermal modeling approach. Second, the graph theory-derived thermal predictions are used as inputs into a finite element model to predict deformation. In other words, we present a hybrid graph theory-finite element model for the prediction of thermal-induced deformation leading to possible recoater crashes.

The central hypothesis is that such a decoupled approach based on using graph theory to obtain the thermal history and the finite element approach to predict deformation will outperform, in terms of computational speed, the coupled thermomechanical finite element model without sacrificing accuracy. We test this hypothesis through verification and experimental validation studies. In these we compare thermal history, deformation in the z-direction (vertical build direction), and recoater crash predictions obtained from the graph theory-based model, with (i) non-proprietary finite element-derived predictions (implemented in Abaqus with identical assumptions), and (ii) a proprietary LPBF modeling software (Netfabb).

Verification results are reported in Chapter 3 for two test parts. Experimental validation of the approach is reported in Chapter 4, in the context of the arch-shaped objects

(with and without supports) exemplified in Figure 2 (top). We note the verification and validation procedure follows the recommendations by Gouge *et al.* in Ref. [22].

Apart from a recoater crash, the deformation of the part during printing is also responsible for another type of common build failure that results from the shearing of anchoring supports. Subsequent to printing, the part may crack or deform when it is separated from the build plate due to thermal-induced residual stresses.

We note that the focus of this work is to predict recoater crashes. We do not report results for part deformation and warpage that occur when the part is removed from the build plate on account of thermal-induced residual stresses. Recoater crashes are caused by superelevation – a phenomenon that is tied to in-process deformation of the part in the z-direction (vertical build direction). Hence, the deformation results reported in this work are restricted to those in the z-direction.

1.3 Literature Review

The thermomechanical finite element (FE) method is a widely used approach for modeling LPBF process to predict thermal-induced residual stress and deformation. The governing principles are based on the concepts of welding [23, 24]. The thermomechanical FE modeling advanced from welding is used to predict thermal history, deformation, and residual stress in LPBF [25-29]. However, there are unique challenges associated with the modeling of LPBF process. The modeling of welding is relatively simpler than the LPBF, wherein welding modeling deals with the process of joining two parts. The part undergoes considerably fewer cycles of heating and cooling, whereas in LPBF several thousand tracks of material are deposited over hundreds of layers. For example, in one cubic inch part typically over 150,000 tracks of material are deposited in 500+ layers, wherein the process

experiences thousands of uneven heating and cooling cycles [24]. Thus, the simulation of this LPBF process has become computationally inefficient and complex.

The fully coupled or decoupled thermomechanical mesoscale modeling of the LPBF process considers the effect of the laser beam as a concentrated, moving body heat source [30, 31]. The mesoscale model demonstrates a high resolution of thermal stress and deformation fields. However, the computational domain is very small, typically several spots, tracks, or layers due to excessive computational expense [30-39]. Hence, researchers investigated simple geometries such as small cubes or thin plates [30, 31, 39-44]. For example, Ma *et al.* [33] developed a transient, two-dimensional axisymmetric FE model to simulate surface melting and solidification resulting from a single laser pulse for studying the effect of pulse duration. They simplified the model by considering homogeneous and isotropic materials while neglecting heat loss due to convection and radiation. The computation domain was as small as $0 < r < 120 \mu\text{m}$ in the radial direction. According to Ma *et al.*, the coupled FE model can be used to study the effect of process parameters [33]. Nickel *et al.* advanced to three-dimensional (3D) FE modeling to study thermal stress and deformation due to deposition patterns [45]. Dai *et al.* used an ANSYS model to simulate the LPBF process to investigate the thermal history and warpage of a layer-by-layer build part, but the result showed only two layers without validation [36].

According to current literature, mesoscale modeling cannot be used in the industrial environment for building large and complex geometries without implementing multi-scaling or layer lumping approach [31, 46, 47]. Hence, researchers seek part-level modeling which enables them to model real-size parts with a reasonable computational expense [31, 48-51]. It has been found that simulating several layers or blocks, instead of

a single track or layer at a time substantially reduced the computational burden. However, part-level modeling requires considering several model simplification assumptions. For instance, Zaeh *et al.* [47] investigated the residual stress and thermal-induced distortion in an LPBF process. They implemented the layer lumping approach also known as a super layer approach in their model. Williams *et al.* [49] studied thermal stress, residual stress, and deformation by simulating blocks of multiple layers. Liang *et al.* [47] investigated the layer lumping approach to accelerate the simulation of metal components in the LPBF process. According to Liang *et al.*, the super layer thickness ranging from 0.4 mm to 0.6 mm reduces the computation time significantly with good accuracy.

Gouge *et al.* [22, 51-53], Luo *et al.* [54], DebRoy *et al.* [55], and Bandyopadhyay *et al.* [16] have recently published comprehensive studies on part-level finite element modeling in AM. Researchers have proposed several strategies to reduce the computational burden of FE analysis. The summary of the strategies are as follows:

1. Mesh refinement technique

In the mesh-based AM process simulation, following every new track or layer of deposition, the whole consolidating part has to be re-meshed. Hence, the computation is usually inefficient and complex. To address this issue (i.e., to reduce the computational cost) researchers have proposed some techniques such as adaptive meshing, inactive element approach, quiet element approach, and hybrid meshing.

- i. Adaptive meshing approach: The key idea of this approach is to create finer mesh at a specific area where boundaries change intensely while keeping coarser mesh for the rest of the part [56]. As a result, computational expense reduces significantly.

Commercial software such as Amphyon and Autodesk Netfabb use adaptive meshing to accelerate the simulation [57].

- ii. Inactive element approach: Elements are incrementally added for each new deposition and only the nodes of the active element are considered during simulation. The number of elements of the parts increases as the part builds up and requires repetitive equation numbering and solver initialization, resulting in an inefficient implementation of this approach. [22].
- iii. Quiet element approach: The concept of this approach is to mesh the entire geometry and assign element properties prior to the simulation. The active elements of the consolidating part are simulated while the rest of the elements have no thermal or mechanical effect. This approach is computationally more efficient than the inactive element approach, as the number of elements remains constant in the entire simulation [22, 56].
- iv. Hybrid meshing approach: This approach combines inactive and quiet element techniques. Initially, the elements are kept inactive. Then before a new layer is activated for simulation, the elements are switched to quiet. This approach is faster than the inactive and quiet element approaches with the same level of accuracy [22]. Commercial software Autodesk Netfabb implemented this approach in its software [56, 58].

2. Model simplification

According to the current literature, the simplification approach is commonly used in AM to reduce the computation. This approach includes geometry simplification through simulating a portion of a symmetric part, simplification of the energy

source by heating the entire layer at once, and simplification of the process physics by ignoring the latent heat of the melt pool phenomena, considering isotropic and homogeneous material properties [33]. However, some of the simplifications can negate the prediction accuracy significantly [56, 59].

Based on the computational strategies, the available thermomechanical models to predict thermal-induced deformation in AM are categorized as follows and shown in Figure 3.

i. Coupled thermomechanical FE model

The key idea of this modeling technique is that the nonlinear thermal and mechanical equations are solved at every time step for the entire simulation to compute the thermal history and mechanical responses such as thermal stress, residual stress, and deformation. The coupled thermomechanical FE model can provide very precise thermal and mechanical solutions. However, the computation cost is high, and simplification assumptions are required in order to simulate large and complex parts. The details of the coupled thermomechanical FE modeling approach can be found in the literature [36, 38, 39, 45, 53, 54, 60-66].

ii. Decoupled thermomechanical FE model

The governing principle of this modeling approach is to perform a thermal simulation of the process and obtain a thermal history, then employ the thermal history to a mechanical model to predict mechanical responses such as thermal stress, residual stress, and deformation. Thermal simulation is independent of mechanical analysis [22]. The benefit of this type of modeling approach is that the computation is faster than coupled thermomechanical approach and provides

reasonable prediction accuracy. However, the decoupled thermomechanical model loses fidelity when the distortion is high enough to change the system boundaries. The modeling approach, benefits, and challenges are discussed in the literature [49, 53, 67-79]. Commercial software such as Autodesk Netfabb, Amphyon, Simufact, and Additive Print implement this approach in their software for AM process simulation and optimization.

iii. Meshfree approach

Despite the different strategies adopted to model the AM process using finite elements, the computational expense is still significant. Hence, researchers have explored meshfree techniques. For example, Yavari *et al.* developed graph theory-based thermal modeling to predict thermal history in the LPBF process [56], Peng *et al.* introduced a thermal circuit network (TCN) model to predict the thermal history of a part, then using the thermal history coupled with FE to predict thermomechanical behavior such as thermal stress, residual stress and distortion [57, 80]. Commercial software Sunata is developed based on the thermal circuit network (TCN) model [57]. Ganeriwala *et al.* developed a coupled discrete finite-difference model to simulate heat transfer for melt pool size prediction [81]. These models are computationally more efficient than the finite element model. However, these models have not been explored rigorously in the broader spectrum of AM processes.

iv. AI-based approach

Researchers have recently implemented an AI-based approach in AM to predict thermal history, residual stress, and thermal-induced distortion. For example,

Chowdhury *et al.*[82] developed an artificial neural network (ANN)-based model to investigate thermal-induced deformation. They used the model prediction to compensate for the geometric dimensional inaccuracy which occurs due to thermal-induced deformation. According to Chowdhury *et al.*, by implementing the ANN-based model, the part dimensional accuracy improved substantially. Francis *et al.* [83] introduced a recurrent neural network (RNN)-based deep learning approach to study thermal-induced distortion in laser-based additive manufacturing (LBAM). This deep learning modeling approach offers automated feature learning and facilitates highly accurate distortion prediction. In addition, it is easily integrable to cloud computing which fits into the industry 4.0 framework for analyzing big data. However, the bottleneck of this approach is that it requires high performance computing (HPC) for training, as well as large physical memory (>100GB).

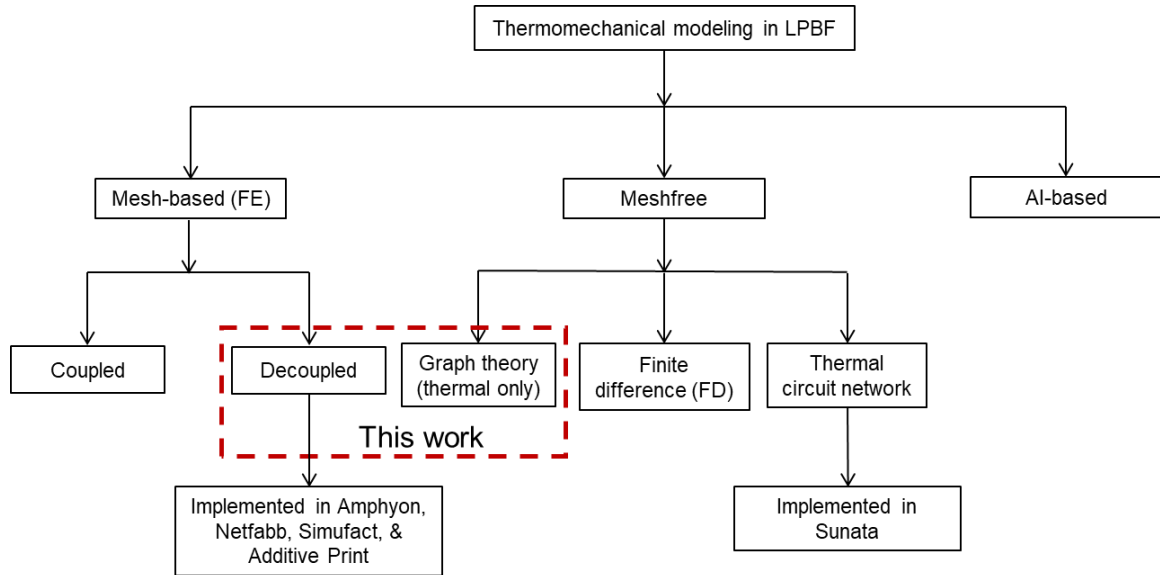


Figure 3: Available thermomechanical modeling approaches to predict thermal-induced deformation are categorized based on the computational technique.

This work makes an effort to develop a computationally efficient thermomechanical model for the LPBF process simulation by coupling sequentially a meshfree, graph theory-based thermal model with a FE mechanical model. The graph theory-based thermal analysis is independent of the FE-based mechanical analysis and vice-versa. Yavari *et al.* [56] have shown that the graph theory thermal model is nearly 10 times faster than the FE model for thermal analysis. Besides, the decoupled thermomechanical model is a widely accepted modeling approach in AM due to its computational efficiency. Hence, to take the advantage of the graph theory thermal model and decoupled modeling approach, we developed the graph theory-based thermomechanical model to predict thermal induced deformation in LPBF. The modeling approach is discussed in detail in the forthcoming Chapter 2.

CHAPTER 2 – APPROACH

The graph theory-based thermomechanical modeling approach consists of two sequential phases. First, the temperature distribution in the part after the end of each layer is predicted using the graph theory thermal model. Second, the mechanical response (i.e., deformation) is obtained by exporting the temperature distribution predictions obtained from graph theory to an FE model. The sequential coupling flow process is shown in Figure 4.

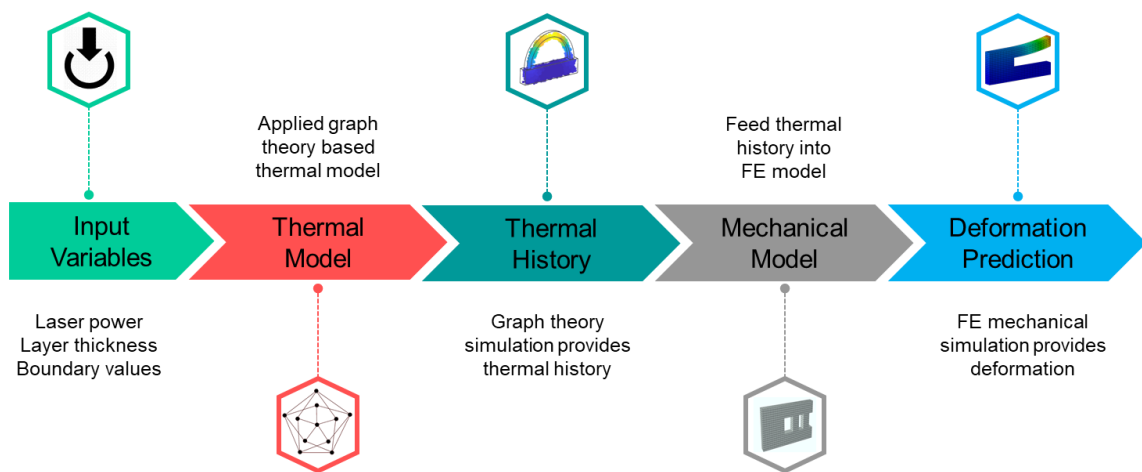


Figure 4: The sequential steps of graph theory-based thermomechanical modeling wherein the graph theory thermal model uses the input parameters to estimate thermal history. Next, the FE-based mechanical model receives the thermal history from the graph theory model and computes thermal-induced deformation.

The rationale for using the graph theory approach for thermal analysis is that it reduces computation time compared to FE analysis. The graph theory approach, by obtaining the temperature distribution over a set of discrete nodes, and its distinct matrix multiplications solution, saves computational effort compared to FE method. In the second phase, the temperature distribution obtained at the end of a layer using the graph theory approach is exported to a finite element mesh of the part, reflecting the part geometry at the end of a layer from which the thermal-induced deformation is obtained.

The decoupled approach implemented in this work assumes that the thermal distribution influences the mechanical response, but the mechanical response does not influence the thermal history. The unidirectional relationship between the thermal and mechanical problems is an assumption that is widely applied in the LPBF field. However, as pointed out by Michaleris *et al.* [22, 52, 53], this assumption would need to be relaxed when the deformation is severe so as to drastically change the part shape or physical constraints, such as the failure of supports and detachment of the part from the build plate.

2.1 Overview of Thermal Modeling in AM using Graph Theory

The temperature distribution of a part being printed in the LPBF process is predicted by solving the continuum heat diffusion equation [52].

$$\overset{\text{Material}}{\text{Properties}} \widehat{\rho c_p} \frac{\partial T(x, y, z, t)}{\partial t} - k \overbrace{\left(\frac{\partial^2}{\partial x^2} + \frac{\partial^2}{\partial y^2} + \frac{\partial^2}{\partial z^2} \right)}^{\text{Laplacian}} T(x, y, z, t) = \overset{\text{Processing}}{\text{Parameters}} \widehat{E_V} \quad (1)$$

Here, the material density is ρ [$\text{kg}\cdot\text{mm}^{-3}$], specific heat c_p [$\text{J}\cdot\text{kg}^{-1}\cdot\text{K}^{-1}$], thermal conductivity k [$\text{W}\cdot\text{m}^{-1}\cdot\text{K}^{-1}$], $T(x, y, z, t)$ is the instantaneous temperature at location (x, y, z) at time t . The second derivative term in the heat equation captures the effect of shape on the temperature distribution. This second derivative is called the *continuous Laplacian* [2]. On the right-hand side is the energy density E_v [$\text{J}\cdot\text{mm}^{-3}$]; $E_v = \frac{P}{v \times h \times t}$ is defined as the amount of energy supplied by the laser to melt a unit volume of powder. The volumetric energy density is a function of laser power (P) [W], laser scanning speed (v) [ms^{-1}], spacing between two consecutive laser tracks (h), [mm], and layer thickness (t), [mm]. To solve the heat diffusion equation the following boundary conditions are typically imposed,

$$T(x, y, z, t = 0) = T_m(x, y, z)$$

$$\frac{\partial T(x, y, z, t)}{\partial n} = 0 \quad (2)$$

In Eq.(2), T_m is the melting point of the material and n is the outward normal vector at the boundary. The heat diffusion equation is further simplified as follows, with the Laplacian operator represented as ∇^2 and the thermal diffusivity as $\alpha = \frac{k}{\rho c_p}$.

$$\frac{\partial T(x, y, z, t)}{\partial t} - \alpha \nabla^2 T(x, y, z, t) = 0 \quad (3)$$

The graph theory approach approximates the continuous Laplacian with the Laplacian matrix L , in effect, $\nabla^2 = -L$. The solution is obtained by discretizing the heat diffusion equation over N nodes and by replacing the continuous temperature with a discrete temperature vector (T),

$$\frac{\partial T(x, y, z, t)}{\partial t} + \alpha L T(x, y, z, t) = 0 \quad (4)$$

The eigenvector matrix (ϕ) and eigenvalue matrix (Λ) of the Laplacian matrix (L) are found by solving the eigenvalue equation $L\phi = \phi\Lambda$.

$$\frac{\partial T(x, y, z, t)}{\partial t} + \alpha(\phi\Lambda\phi^{-1}) T(x, y, z, t) = 0 \quad (5)$$

As the Laplacian matrix is symmetric and positive semi-definite, as described later in Chapter 2.2, the eigenvalues (Λ) are non-negative, and the eigenvector matrix (ϕ) is orthogonal [84-87]. As the transpose of an orthogonal matrix is the same as its inverse, that is, $\phi^{-1} = \phi'$, making substitution in Eq. (5) gives,

$$\frac{\partial T(x, y, z, t)}{\partial t} + \alpha(\phi\Lambda\phi') T(x, y, z, t) = 0 \quad (6)$$

Equation (5) is a first-order, ordinary linear differential equation, with solution [61],

$$T(x, y, z, t) = e^{-\alpha(\phi\Lambda\phi')t} T_m \quad (7)$$

The term $e^{-\alpha(\phi\Lambda\phi')t}$ is simplified via a Taylor series expansion and substituting $\phi\phi' = I$,

$$\begin{aligned}
e^{-\alpha(\phi\Lambda\phi')t} &= I - \frac{\phi\Lambda\alpha t\phi'}{1!} + \frac{(\phi\Lambda\alpha t\phi')^2}{2!} - \frac{(\phi\Lambda\alpha t\phi')^3}{3!} + \dots \\
&= I - \frac{\phi\Lambda\alpha t\phi'}{1!} + \frac{(\phi\Lambda\alpha t\phi')(\phi\Lambda\alpha t\phi')}{2!} - \frac{(\phi\Lambda\alpha t\phi')(\phi\Lambda\alpha t\phi')(\phi\Lambda\alpha t\phi')}{3!} + \dots \\
&= I - \frac{\phi\Lambda\alpha t\phi'}{1!} + \frac{\phi'(\Lambda\alpha t)^2\phi'}{2!} - \frac{\phi(\Lambda\alpha t)^3\phi'}{3!} + \dots
\end{aligned} \tag{8}$$

$$e^{-\alpha(\phi\Lambda\phi')t} = \phi e^{-\alpha(\Lambda)t} \phi'$$

$$\text{Substituting, } e^{-\alpha(\phi\Lambda\phi')t} = \phi e^{-\alpha\Lambda t} \phi' \text{ into Eq. (7) gives,} \tag{9}$$

$$T(x, y, z, t) = \phi e^{-\alpha\Lambda t} \phi' T_m$$

Equation (9) is the graph theory solution to the discrete heat diffusion equation as a function of the eigenvalues (Λ) and eigenvectors (ϕ) of the Laplacian Matrix (L), constructed on a discrete set of nodes. The graph theory (Thermal) approach has two inherent advantages over FE analysis.

- (1) *Elimination of mesh-based analysis.* The graph theory (Thermal) approach represents the part as discrete nodes, which entirely eliminates the tedious meshing steps of FE analysis.
- (2) *Elimination of matrix inversion steps.* While FE analysis rests on matrix inversion at each time step for solving the heat diffusion equation, the graph theory (Thermal) approach relies on matrix multiplication, shown in Eq. (9), which greatly reduces the computational burden.

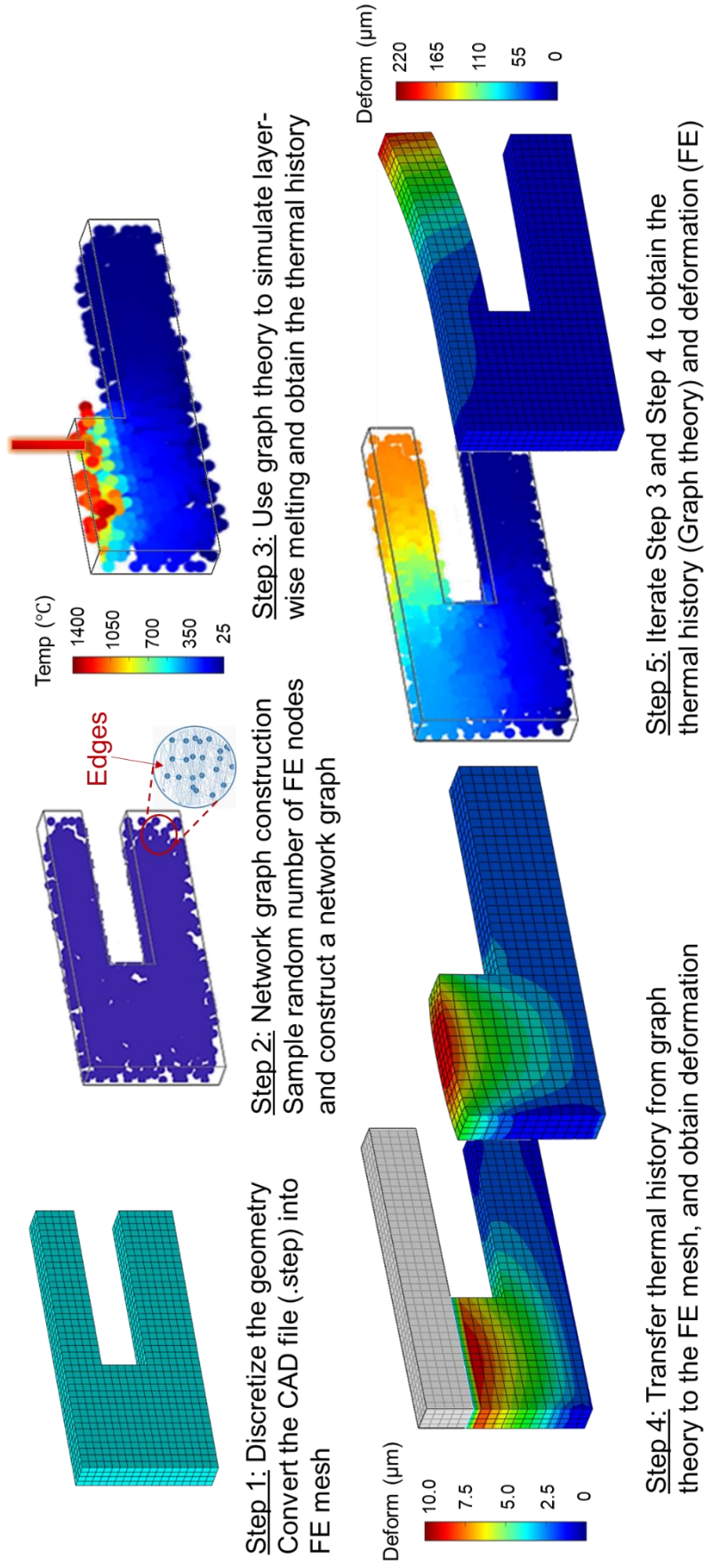


Figure 5: Schematic representation of graph theory approach in the context of the L-PBF process. The key to the process is to determine the thermal history of the part using graph theory thermal modeling. This information is then transferred to finite element analysis to determine thermal-induced deformation.

2.2 Thermomechanical Analysis using Graph Theory and Finite Element Modeling

The manner in which the graph theory approach is adapted for thermal modeling in LPBF, and subsequently combined with finite element modeling, is described in Steps 1 through 4.

Step 1: Discretization of the geometry into nodes

The entire (desired) part geometry, in the form of a STEP file, is transformed into a FE mesh which also generates a set of discrete nodes. The position of these nodes is recorded in terms of their spatial coordinates (x, y, z) .

Step 2: Network graph construction

A fixed number of N nodes are sampled randomly from the FE-generated nodes obtained from Step 1. In this work, the random sampling is adjusted such that a constant volumetric density of nodes ($n \text{ nodes} \cdot \text{mm}^{-3}$) is selected. These nodes are then used in Steps 2 through 3 to obtain the thermal history using graph theory. The temperature history of the node located at (x, y, z) at a simulation time step Δt is $T(x, y, z, \Delta t)$. The spatiotemporal temperature distribution obtained from graph theory simulation for the whole part is stored in a tensor \mathbf{T} .

The N randomly sampled nodes obtained from step 1, are binned into their respective layers and a network graph is constructed by connecting these nodes based on their spatial distance. The link connecting the nodes is known as an edge. Nodes in layers where the material is deposited are termed active nodes, and those nodes that belong in layers that are yet to be deposited are termed inactive nodes.

Consider an active node π_i at the center of a sphere of radius ε (mm). The active nodes that fall inside or on the surface of the sphere are called the neighbors of π_i . The radius of the sphere is termed as *neighborhood distance* (ε) and is a tunable parameter. The neighborhood distance is chosen based on the geometry of the part to be modeled. A guideline is to set the neighborhood distance no greater than the dimension of the finest feature in a part [56]. In this work, we set $\varepsilon = 2$ mm for all parts studied.

To reduce the computation burden and avoid the non-physical effects of connecting nodes that are far away from each other, we only connect a fixed number of nearest nodes within the ε -neighborhood of a node. In other words, node π_i is connected to certain nearest nodes within its ε -neighborhood. For example, we connect the node π_i to its fifteen nearest nodes with an edge in C-shaped parts.

Next, the Euclidean distance between two connected nodes (e.g., node π_i and a node π_j whose spatial Cartesian coordinates are $c_i(x_i, y_i, z_i)$ and $c_j(x_j, y_j, z_j)$, respectively) is computed, and weight $a_{i,j}$ is assigned to each edge based on the Gaussian function (also called the heat kernel),

$$\begin{aligned}
 d(c_i, c_j) &= \|c_i - c_j\|^2 = (x_i - x_j)^2 + (y_i - y_j)^2 + (z_i - z_j)^2 . \\
 a_{i,j} &= e^{-\frac{d(c_i, c_j)}{\sigma^2}} \quad \forall i \neq j, d(c_i, c_j) \leq \varepsilon \\
 &= 0, \text{ otherwise} \\
 \lim_{c_i - c_j \rightarrow 0} a_{i,j} &= 1
 \end{aligned} \tag{10}$$

In other words, nodes beyond the neighborhood distance are not connected and no node is allowed to connect to itself. Further, the edge weight depends on the relative distance between the nodes and is between 0 and 1. The larger the edge weight between two nodes, the proportionally greater is the heat transfer between them. The quantity σ^2 in Eq. (10) is the variance obtained from the standard deviation of the Euclidean distance $d(c_i, c_j)$ between all node pairs.

Next, an adjacency or similarity matrix is formed by placing $a_{i,j}$ in row i and column j ,

$$A = [a_{i,j}].$$

$$A = \begin{bmatrix} 0 & a_{1,2} & a_{1,3} & \cdots & a_{1,N} \\ a_{2,1} & 0 & a_{2,3} & \cdots & a_{2,N} \\ a_{3,1} & a_{3,2} & 0 & \cdots & a_{3,N} \\ \vdots & \vdots & \vdots & \ddots & \vdots \\ a_{N,1} & a_{N,2} & a_{N,3} & \cdots & 0 \end{bmatrix} \quad (11)$$

The adjacency matrix is an $N \times N$ symmetric matrix, hence, $a_{i,j} = a_{j,i}$, where N represents the number of randomly sampled nodes. A degree matrix, D is formed by summing the rows of the adjacency matrix A and placing the sums in the i^{th} diagonal. The diagonal entries $d_{i\cdot}$ are positive and off-diagonal entries are zero.

$$d_{i\cdot} = \sum_{j=1}^N a_{i,j}$$

$$D = \begin{bmatrix} d_{1\cdot} & 0 & 0 \\ 0 & \ddots & 0 \\ 0 & 0 & d_{N\cdot} \end{bmatrix} \quad (12)$$

The discrete graph Laplacian matrix is constructed as

$$L = D - A$$

$$L = \begin{bmatrix} +d_{1\cdot} & -a_{1,2} & -a_{1,3} & \cdots & -a_{1,N} \\ -a_{2,1} & +d_{2\cdot} & -a_{2,3} & \cdots & -a_{2,N} \\ -a_{3,1} & -a_{3,2} & +d_{3\cdot} & \cdots & -a_{3,N} \\ \vdots & \vdots & \vdots & \ddots & \vdots \\ -a_{N,1} & -a_{N,2} & -a_{N,3} & \cdots & +d_{N\cdot} \end{bmatrix} \quad (13)$$

The Laplacian matrix falls under the category of a Stieltjes matrix as all its elements are real, it is symmetric and diagonally dominant with all off-diagonal elements non-positive. The Laplacian matrix is positive semi-definite. From the Laplacian matrix, eigenvalues (Λ) and eigenvectors (Φ) are obtained by solving the eigenvalue problem $L\Phi = \Phi\Lambda$ with standard methods.

Step 3: Simulate layer deposition and predict the temperature distribution

In this step, in every cycle, a new layer is deposited on the top of the previously deposited layers at its melting temperature. The heat on the top layer diffuses to the rest of the part via edges connecting the various nodes. The temperature at each node is determined at each time step Δt and stored in the temperature vector $T(x, y, z, \Delta t)$.

The time between layers (TBL) is the time between the start of laser scanning of one layer to the start of scanning the next consecutive layer; it is the sum of the time it takes to scan a layer and recoat a fresh layer. For simulation, the TBL is divided into small timesteps Δt .

The temperature at a node $T(x, y, z, \Delta t)$ at time step Δt is a function of eigenvectors (ϕ) and eigenvalues (Λ) of the Laplacian matrix (L), determined by solving the first-order linear differential equation as discussed in Eq. (9).

$$T(x, y, z, \Delta t) = \phi e^{-\alpha g \Delta t} \phi' T_m(x, y, z) \quad (14)$$

In this work, T_m is the melting point of Inconel 718, $T_0 = \sim 1400$ °C. To reduce the computational burden, we simulate the deposition and melting of several layers. This technique called the super layer or meta-layer approach is commonly used in LPBF as it reduces the simulation time, compared to a layer-by-layer approach while without drastically degrading computational accuracy [48, 49, 88, 89].

To adjust the units to the solution of the heat equation, a parameter called gain factor g is introduced in Eq. (14). The effect of the gain factor g is discussed in depth in our previous work; it influences the diffusion rate. The gain factor is contingent on the material type and node density. In this work, we set $g = 2 \times 10^6$ m⁻². This value is identical to those used in our previous work with Inconel 718 [90].

In Eq. (14) the temperature of a node $T(x, y, z, \Delta t)$ is obtained by incorporating only the conduction heat loss of the part to the substrate. Heat loss due to convection and radiation occurs at the boundary nodes; this is factored using a lumped capacitive theory,

$$T_b = e^{-\tilde{h}\tau} (T_{bi} - T_p) + T_p \quad (15)$$

Here, the temperature of the surroundings T_p is considered as constant, T_{bi} is the boundary node temperature obtained by the heat diffusion alone in Eq. (14), T_b is the resulting boundary node temperature incorporating convection and radiation heat loss, τ is the dimensionless time between layer depositions, and \tilde{h} is the normalized cumulative coefficient of heat loss for convection (via Newton's law of cooling) and radiation (via Stefan-Boltzmann law) from the boundary nodes to the surrounding powder and air.

After convection and radiation are adjusted at boundary nodes, the temperature at various nodes obtained from graph theory at each node located at position (x, y, z) at time step Δt is $T(x, y, z, \Delta t)$. This spatiotemporal temperature distribution over time is stored as a matrix tensor \mathbf{T} .

Step 4: Mechanical analysis using finite element method

Step 4 is the bridge between the thermal history obtained using graph theory and the mechanical analysis from FE. The temperature (thermal history) at each node at the end of each layer stored in the tensor \mathbf{T} from step 3 is mapped (transferred) to its exact location on the FE mesh of the part generated in Step 1 for mechanical analysis. Since the focus of this work is to predict recoater crashes, which occur when the deformation in the top layer of a part exceeds the layer thickness ($40 \mu\text{m}$), we assume that elastic and thermal-induced strains dominate, and plastic strain is ignored. These assumptions are used frequently by LPBF researchers in the literature [91, 92].

Based on small deformation theory, as elucidated by Gouge *et al.* [22], this approach is valid when there are no major faults, such as cracking, the collapse of the supports, and separation of the part from the build plate. Such failures would not only alter the shape of the part but also change the heat conduction pathway, leading to considerable changes in the temperature profile.

In FE analysis, the thermal-induced deformation $\{U\}$ is computed according to the following equations for elastic materials [57, 93]. The bottom face of the part is considered to be constrained (attached) to the substrate. A combination of displacement and traction boundary conditions is enforced to the entire part. The bottom face is in a fixed condition

(i.e., $u = v = w = 0$) which means displacements in x, y, and z directions are zero. Where u, v, and w are the displacement components in x, y, and z directions. Traction boundary conditions $T^{(n)}$ is enforced at the specific nodes using thermal history. Moreover, the free surfaces (i.e., the surfaces between part and powder, and the top surface) are given traction free conditions, $T^{(n)} = 0$.

The deformation of a node is obtained according to Eq. (16)

$$\{U\} = [K]^{-1}\{F_T\} \quad (16)$$

where $\{U\}$ is the displacement vector; $[K]$ the element stiffness matrix; and $\{F_T\}$ is the thermal load vector. These are obtained per Eq. (17) and Eq. (18),

$$[K] = \int [B]^T [H] [B] \cdot dv \quad (17)$$

$$\{F_T\} = \int [B]^T [H] \alpha (\Delta T) \cdot dv \quad (18)$$

Where the domain of integration is the volume of an element, $[B]$ is the strain-displacement matrix, $[H]$ is the elasticity matrix, α is the vector of thermal expansion coefficients, and ΔT is the temperature difference between two nodes. For linear elastic isotropic materials, the elasticity matrix $[H]$ is given by Eq. (19).

$$[H] = \frac{E}{(1+\nu)(1-2\nu)} \begin{bmatrix} 1-\nu & \nu & \nu & 0 & 0 & 0 \\ \nu & 1-\nu & \nu & 0 & 0 & 0 \\ \nu & \nu & 1-\nu & 0 & 0 & 0 \\ 0 & 0 & 0 & \frac{1-2\nu}{2} & 0 & 0 \\ 0 & 0 & 0 & 0 & \frac{1-2\nu}{2} & 0 \\ 0 & 0 & 0 & 0 & 0 & \frac{1-2\nu}{2} \end{bmatrix} \quad (19)$$

where E is the modulus of elasticity [$\text{N}\cdot\text{m}^{-2}$] and ν is the Poisson's ratio. The strain-displacement matrix $[B]$ depends on the shape of the finite element used for analysis. In this study, we used eight-node hexahedral elements. The strain-displacement matrix for a hexahedral element is given by Eq. (20). This 8 node hexahedral mesh was chosen, as it is also used in the popular commercial LPBF simulation software, Netfabb.

$$[B] = [B_1 \quad B_2 \quad B_3 \quad B_4 \quad B_5 \quad B_6 \quad B_7 \quad B_8]$$

$$[B_i] = \begin{bmatrix} \frac{\partial N_i}{\partial x} & 0 & 0 \\ 0 & \frac{\partial N_i}{\partial y} & 0 \\ 0 & 0 & \frac{\partial N_i}{\partial z} \\ 0 & \frac{\partial N_i}{\partial z} & \frac{\partial N_i}{\partial y} \\ \frac{\partial N_i}{\partial z} & 0 & \frac{\partial N_i}{\partial x} \\ \frac{\partial N_i}{\partial y} & \frac{\partial N_i}{\partial x} & 0 \end{bmatrix} \quad (20)$$

where N_i is the shape function and is computed by Eq. (21).

$$N_i = \frac{1}{8} (1 + \xi \xi_i)(1 + \eta \eta_i)(1 + \zeta \zeta_i) \quad (21)$$

where ξ_i, η_i and ζ_i denote the natural coordinates of node i , and $i = 1, 2, 3, \dots, 8$.

In this analysis, it is assumed that the mechanical properties of the part are isotropic, and the elastic material behavior is considered only. Interpolation is used to scale temperature-dependent material properties between the build chamber temperature and the melting point.

Step 5: Obtain the thermal history and deformation for the entire part

Steps 3 and 4 are repeated until the entire part is finished, noting that the subsequent layers are simulated as being deposited on top of the previously deposited and deformed layer. Hence, the deformation of subsequent layers accounts for, and is in turn influenced by, dislocations in previous layers.

CHAPTER 3 – VERIFICATION WITH FINITE ELEMENT METHOD

3.1 Procedure

We applied the graph theory-based approach to predict deformation in the z-direction in two LPBF test parts (Figure 6). The verification procedure pertains to comparing both the thermal history and mechanical deformation predictions obtained from the decoupled solution from the proposed graph theory-based approach with: (i) a coupled thermomechanical FE model implemented in Abaqus, and (ii) the commercial software Autodesk Netfabb. We reiterate that the focus of this study is to predict recoater crashes. Since recoater crashes are caused by part deformations in the z-direction (build direction) that occur as the part is being printed (during the process), this work reports deformation in the vertical build direction (z-direction). However, we note that the approach predicts deformations in all three dimensions.

The coupled thermomechanical FE-based simulation serves as the ground truth to calibrate as well as evaluate the graph theory results. The comparison of the graph theory solution and the coupled thermomechanical FE solution is made in terms of the root mean squared error (RMSE) and mean absolute percentage error (MAPE) of the deformation predictions.

The coupled thermomechanical FE model was obtained using the DFLUX routine in Abaqus per the procedure widely used in the LPBF literature (e.g., see Ref. [94, 95]). The mechanical analysis phase of the graph theory approach is identical to the corresponding coupled thermomechanical FE-based analysis. Identical assumptions were imposed in both the coupled thermomechanical FE-based model and graph theory model, including the use of super-layers or meta-layers to ease the computational burden [48]. The meta-layer or

super-layer approach assumes the deposition of multiple layers at once. Both models also maintain identical mechanical boundary conditions and hexahedral mesh elements. In the graph theory (Deformation) model, the mechanical analysis employs the mesh element C3D8R in Abaqus (8-node linear brick, reduced integration, hourglass control). The coupled thermomechanical FE analysis uses the similar C3D8T mesh element (8-node thermally coupled brick, trilinear displacement, and temperature). We note that both element types are identical in shape, except that C3D8R does not facilitate thermal analysis.

Verification with Netfabb was reported with respect to deformation at the top layer of the part. We note the following characteristics inherent to Netfabb which prevent a rigorous one-to-one comparison with either coupled thermomechanical FE or graph theory (Deformation) approaches.

- (i) In Netfabb the user cannot control precisely the number of elements. Four levels of mesh fineness can be selected by the user, these are Fastest, Fast, Accurate, and Most Accurate.
- (ii) Netfabb uses an adaptive meshing strategy for purposes of computational efficiency. The element size in Netfabb is not static but changes continually. The elements in prior layers are made larger (coarser). Hence, it is not possible to track the temperature and deformation at a specific location with Netfabb.
- (iii) In Netfabb the time step for simulation and the time between layers, also called the interlayer time, cannot be controlled by the users. The time between layers is a particularly important factor in determining the thermal history. The time between layers is not constant, but changes during the build in proportion to the surface area to be scanned. A longer time between layers allows a longer time for the part to

cool. The time between layers is automatically determined in Netfabb without user input.

3.2 Test Parts

To verify the graph theory-based solution with the coupled thermomechanical FE model two test parts were considered as shown in Figure 6. These are termed the C-shaped part without supports, Figure 6(a) and the C-shaped part with supports, Figure 6(b). The C-shaped part without supports in Figure 6(a) has a large overhang feature, whose underside is not supported. The overhang region tends to accumulate heat leading to thermal-induced deformation, often leading to a recoater crash.

The C-shaped part built with supports, Figure 6(b), would have a significantly different thermal history from the C-shaped part without supports. This is because the supports would facilitate the conduction of heat away from the overhang region, thus reducing its tendency to deform during printing.

We note that the coupled thermomechanical FE model converged within a minute for these case studies, given the small size and simple shape of the parts. The computation time was increased for the experimental cases in Chapter 4.

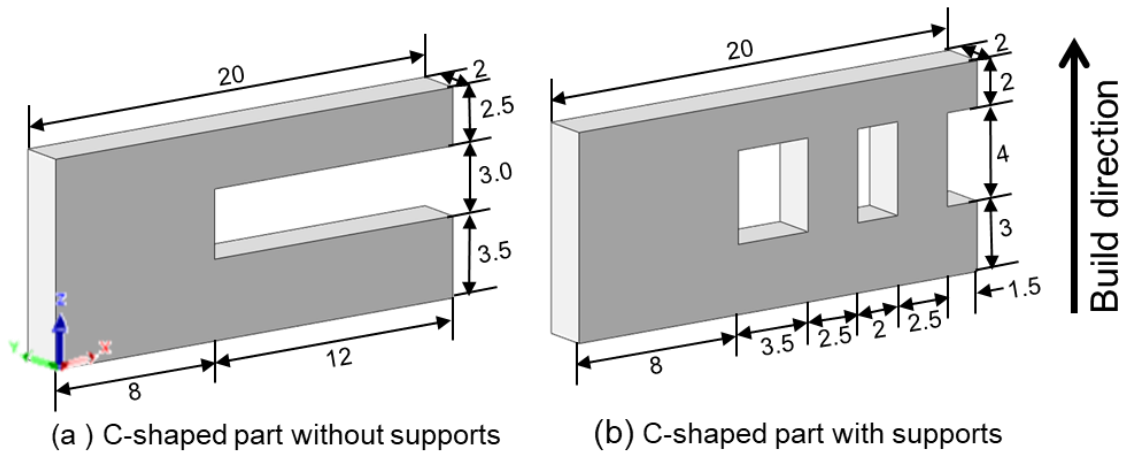


Figure 6: (a) C-shaped part without supports, (b) C-shaped part with supports.

The practical context of using the C-shaped parts as exemplar objects is illustrated in Figure 7, which shows an LPBF knee implant. To prevent the part from collapsing under its own weight, supports were built under the overhanging feature. However, these supports were too thin to prevent heat retention in the overhang region. Hence, after the build, the overhang area manifested overheating, resulting in coarse-grained microstructure and poor surface finish, which made the implant potentially unsafe for clinical use.

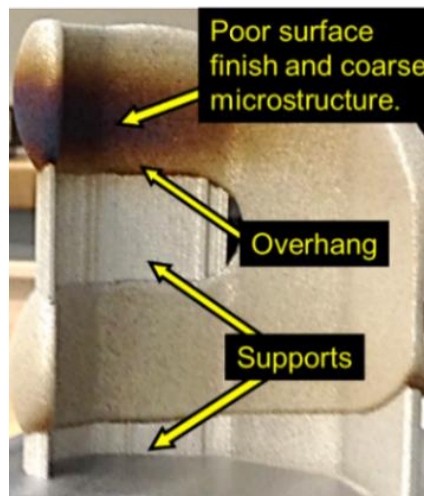


Figure 7: LPBF knee implant with thin supports showing over the heated surface at the overhang region. Image from Yavari *et al.* [6].

3.3 Model Calibration and Convergence

The simulation parameters, material properties are shown in Table 1. The powder properties used in this analysis are of Inconel 718.

Table 1: Summary of material properties and simulation parameters for graph theory and the coupled thermomechanical FE models.

Material properties and simulation parameters	Values
Material	Inconel 718
Density, ρ [$\text{kg}\cdot\text{m}^{-3}$]	8,230
Thermal conductivity, k [$\text{W}\cdot\text{m}^{-1}\cdot\text{K}^{-1}$]	11.1
Specific heat, C_p [$\text{J}\cdot\text{kg}^{-1}\cdot\text{K}^{-1}$]	435
Thermal diffusivity (α) [m^2s^{-1}]	3.2×10^{-6}
Expansion coefficient [$^{\circ}\text{C}^{-1}$]	12.1×10^{-6}
Young's modulus [$\text{N}\cdot\text{m}^{-2}$]	2×10^{11}
Poisson's ratio	0.3
Melting Point (T_m) [$^{\circ}\text{C}$]	1,400
Build chamber temperature, T_{amb} [$^{\circ}\text{C}$]	110
Convection coefficient wall to powder, h_w [$\text{W}\cdot\text{m}^{-2}\cdot\text{C}^{-1}$]	25 (C-shaped parts) 15 (arches)
Convection coefficient substrate (sink), h_s [$\text{W}\cdot\text{m}^{-2}\cdot\text{C}^{-1}$]	5000 (C-shaped parts), 2500 (arches)
Characteristic length [mm]	3
Neighborhood distance (ϵ) [mm]	2
Fixed number of nearest neighbors (n)	15 (C-shaped parts) 5 (arches)
Layer thickness [mm]	0.040
Super layer thickness [mm]	0.5
Gain factor (g) [m^{-2}]	2×10^6
Time between layers [sec]	10 sec for both C-shaped parts, varies for arches based on experiment
Computational hardware	Intel(R) Core (TM) i5-7500 CPU @ 3.40GHz with 16 GB RAM

The model calibration was performed based on the C-shaped part without supports and followed the recommendations of Gouge *et al.* [22, 52, 53]. First, the thermal history

predictions (thermal solution) obtained from graph theory were verified with its corresponding thermal solution obtained from the coupled thermomechanical FE simulation. Next, the thermal solution from graph theory was used as an input to the decoupled mechanical FE model to predict layer-by-layer deformation. The mechanical solution was verified with the coupled thermomechanical FE-based simulation. In effect, the coupled thermomechanical FE model served as the ground truth.

Two parameters need to be calibrated in the graph theory-based model. With super layer thickness fixed at 0.5 mm based on prior work, the first parameter is the number of nodes per unit volume in graph theory (node density, nodes \cdot mm⁻³) for thermal analysis. The second parameter is the FE mesh element size for the prediction of deformation. We note that an extensive convergence study for the coupled thermomechanical FE model was conducted to ascertain the element size. Five element sizes were studied, ranging from 2 mm \times 2 mm \times 2 mm to 0.3 mm \times 0.3 mm \times 0.3 mm, as summarized in Table 2.

The results in Figure 8 show the thermal history and maximum deformation in the z -direction (build direction) as a function of the layer height at a specific location ($x = 4$ mm, $y = 1$ mm, z mm) on the C-shaped part without supports; the origin is on the left front vertex of the part. The result obtained using the graph theory (red line) is overlaid on the temperature and deformation predictions from the coupled thermomechanical FE simulation (ground truth, black line), in Figure 8(a) and Figure 8(b), respectively.

The results in Figure 8(a) show that the surface temperature predictions obtained from the graph theory thermal model converge to the coupled thermomechanical FE solution with the increase of the node density. Increasing the node density is advantageous to prediction accuracy as shown in recent work at the expense of the computation time [56].

The thermal history predictions at the end of each layer obtained from graph theory were imported into an FE model to obtain the mechanical solution. With the decrease in element size, model accuracy improves as is evident in Figure 8(b). As there is a tradeoff between the element size and the computation time, an element size of $0.5 \text{ mm} \times 0.5 \text{ mm} \times 0.5 \text{ mm}$ was considered in this work based on convergence studies. The top surface temperature at a specific spatial location after completion of a layer was predicted using the graph theory approach. The solution was calibrated with respect to the temperature predicted by the coupled thermomechanical FE model as a function of the node density ($\text{nodes} \cdot \text{mm}^{-3}$) with mesh size was set at $0.5 \text{ mm} \times 0.5 \text{ mm} \times 0.5 \text{ mm}$. Based on the calibration, we selected the node density as 5.0 ($\text{nodes} \cdot \text{mm}^{-3}$) that yields MAPE $\sim 1\%$ and RMSE $\sim 7 \text{ }^\circ\text{C}$ with respect to the coupled thermomechanical FE model.

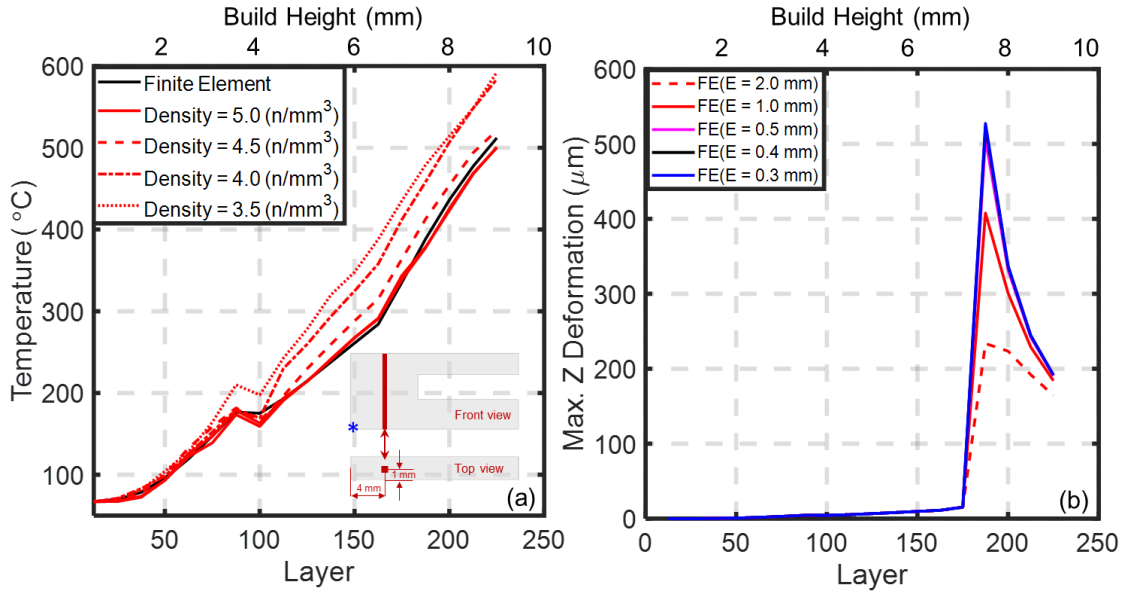


Figure 8: Calibration of (a) graph theory thermal model for node density as the number of nodes per mm^3 and (b) coupled thermomechanical FE model for mesh element size in mm. In the graph theory thermal model, increasing the node density results in better convergence while in coupled thermomechanical FE model, reducing the element size improves the prediction accuracy. In this work, we selected the node density $5.0 \text{ nodes} \cdot \text{mm}^{-3}$ and mesh element size 0.5 mm. The asterisk* represents the origin ($x = 0, y = 0, z = 0$) of the C-shaped parts.

Table 2: Effect of the number of nodes on graph theory thermal prediction and element size on deformation prediction using FE.

Variables	Number of nodes	MAPE (%)	RMSE ($^{\circ}\text{C}$)	Computation time (s)
Thermal history	1540 (selected)	1	7	11
	1295	3	17	10
	1230	6	48	9
	1080	9	62	8
Deformation	Element size (mm)	MAPE (%)	RMSE (μm)	Computation time (s)
	$2 \times 2 \times 2$	8	76	6
	$1 \times 1 \times 1$	3	30	16
	$0.5 \times 0.5 \times 0.5$ (selected)	1	5	57
	$0.4 \times 0.4 \times 0.4$	0.15	1	92
	$0.3 \times 0.3 \times 0.3$	0	0	756

3.4 C-shaped Part without Supports

The part geometry as shown in Figure 6(a) was converted into FE mesh. The mesh consisted of 2,624 elements (3705 nodes) having an approximate element size of $0.5 \text{ mm} \times 0.5 \text{ mm} \times 0.5 \text{ mm}$. These nodes were extracted from the FE model and employed in the graph theory model for predicting deformation, as described in Steps 2 through 5 in Chapter 2.

3.4.1 Thermal History Prediction

The temperature predictions from the graph theory approach were obtained with node density set at $5 \text{ nodes} \cdot \text{mm}^{-3}$. Shown in Figure 9(a) is the average surface temperature prediction at the end of the layer. Likewise, reported in Figure 9(b) and Figure 9(c) are the surface temperature at the specific location ($x = 4 \text{ mm}$, $y = 1 \text{ mm}$, $z \text{ mm}$) and location ($x = 7 \text{ mm}$, $y = 1 \text{ mm}$, $z \text{ mm}$), respectively. The temperature predictions using the graph theory (red line) overlaid on the temperature predictions from the coupled thermomechanical FE simulation (ground truth, black line).

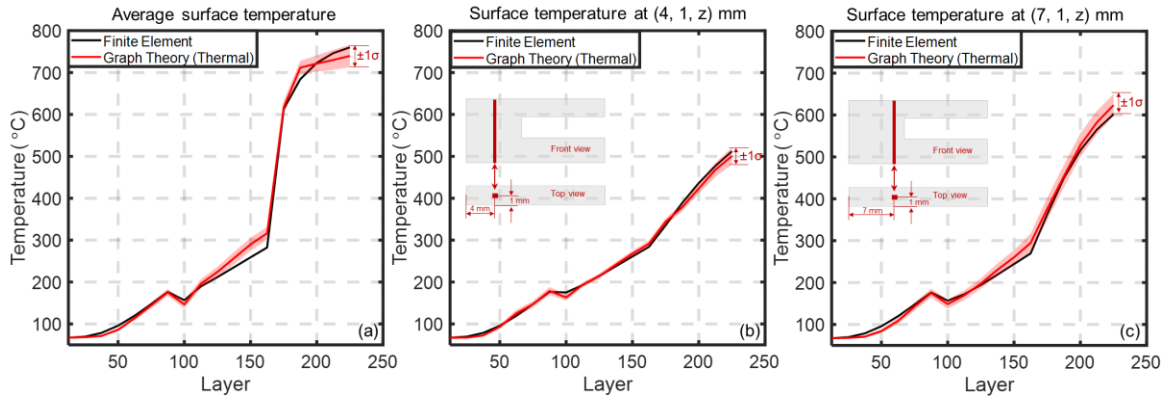


Figure 9: Thermal history of the C-shaped part without supports. (a) Average surface temperature measured at the end of the layer. (b) & (c) Surface temperature at a specific location (4, 1, z) mm and (7, 1, z) mm, respectively. The red line in the figure represents the thermal history predicted using the graph theory approach with ± 1 standard deviation over 10 replications, whereas the black line is the thermal history predicted using the coupled thermomechanical FE model which is considered as the ground truth.

The error in the graph theory thermal prediction with respect to the coupled thermomechanical FE model for the average surface temperature in Figure 9(a) is $\sim 2\%$ (MAPE) and ~ 16 °C (RMSE). Similarly, for the chosen location ($x = 4$ mm, $y = 1$ mm, z mm) reported in Figure 9(b) the MAPE and RMSE are $\sim 1\%$ and ~ 7 °C, respectively, and at location ($x = 7$ mm, $y = 1$ mm, z mm) reported in Figure 9(c) the MAPE and RMSE are $\sim 2\%$ and ~ 12 °C, respectively. The graph theory thermal prediction is bounded with ± 1 standard deviation over ten replications. The graph theory thermal simulation converged in ~ 6 seconds while the coupled thermomechanical FE reached the solution in ~ 58 seconds. The temperature distribution of the complete part obtained from the coupled thermomechanical FE, graph theory (Thermal), and Netfabb simulations is shown in Figure 10.

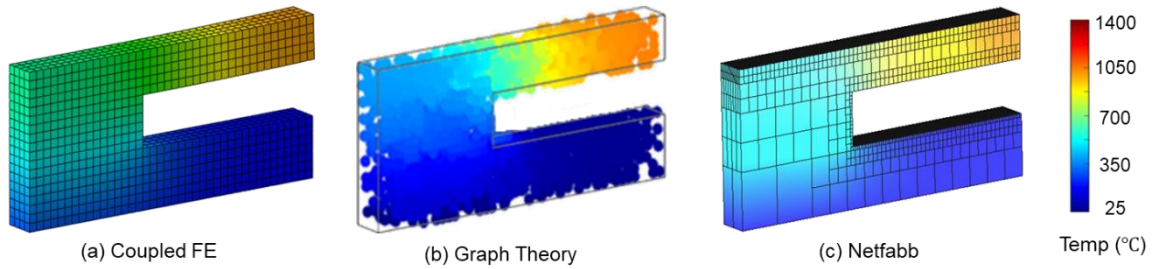


Figure 10: Qualitative comparison of thermal history predictions at the completion of the part from (a) coupled thermomechanical FE model, (b) graph theory (Thermal) model, and (c) Netfabb.

3.4.2 Deformation Prediction

The maximum top surface deformation predicted using the graph theory-based approach is shown in Figure 11(a), and closely tracks the deformation obtained from the coupled thermomechanical FE simulation. The results are summarized in Table 3 and Table 4. The average deformation in each layer is shown in Figure 11(b). Next, shown in Figure 11(c) & Figure 11(d) are the deformations as a function of layer height at the specific locations (4 mm, 1 mm, z mm) and (7 mm, 1 mm, z mm), respectively. Layers 188 - 225 undergo considerable deformation due to heat accumulation in the overhang region. From Figure 11(a) and Figure 11(b), we note that the deformation in the z-direction exceeds the layer thickness ($40 \mu\text{m}$) at a build height of 7 mm, indicating the possibility of a recoater crash. In these studies, the typical error in the graph theory (Deformation) approach with respect to the coupled thermomechanical FE model is $\sim 4\text{-}6\%$ (MAPE) and $\sim 0\text{-}9 \mu\text{m}$ (RMSE).

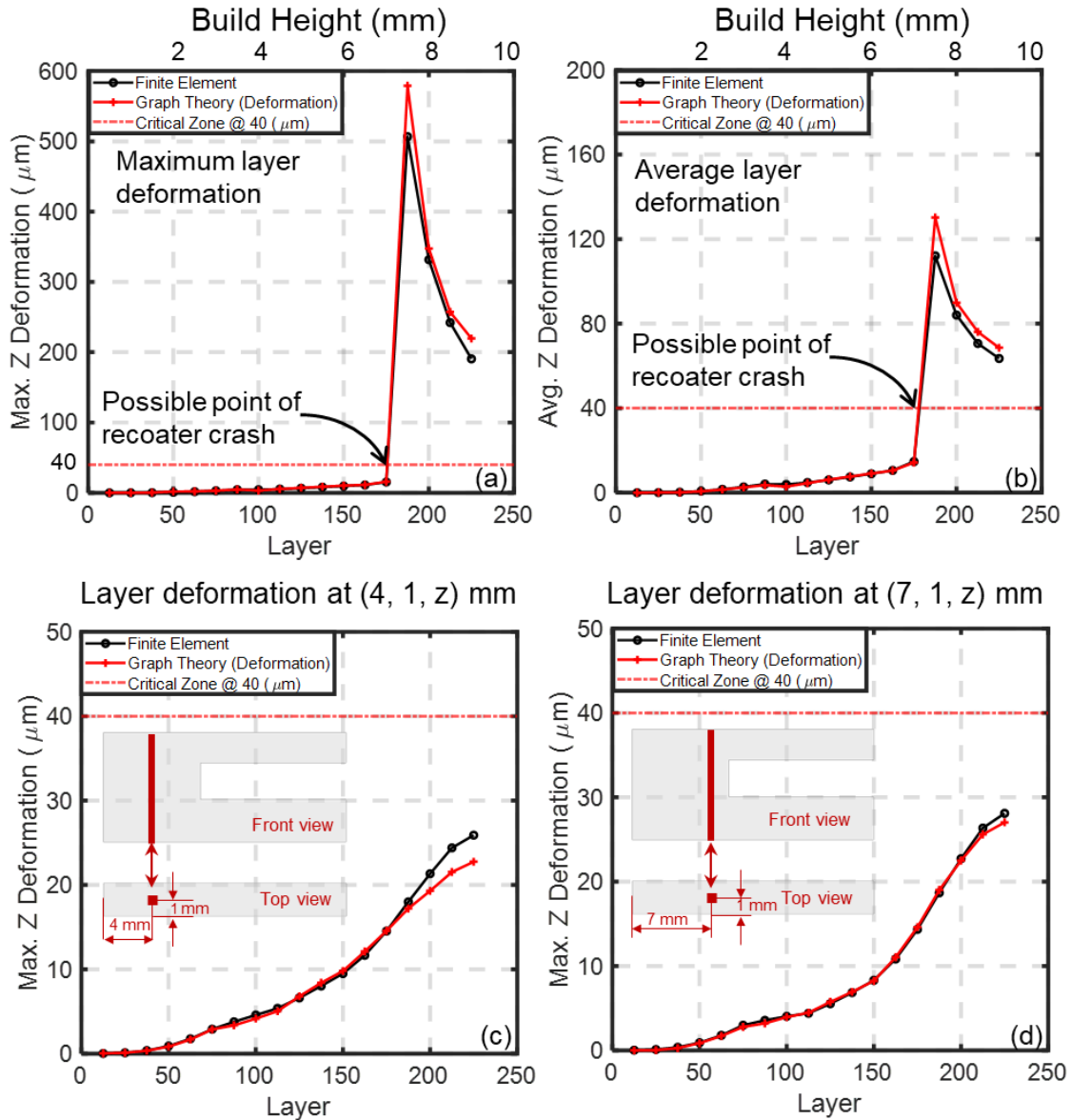


Figure 11: Comparison of predicted deformation of C-shaped part without supports between the coupled thermomechanical FE model and the graph theory-based approach showing (a) maximum deformation of each layer, (b) average layer deformation, and (c) & (d) deformation measured at (4, 1, z) mm, and (7, 1, z) mm, respectively, along the build direction.

Table 3: Graph theory (Deformation) model performance in terms of MAPE, RMSE, and computation with respect to coupled thermomechanical FE model. The MAPE and RMSE are estimated based on the maximum deformation of each layer.

Part	Variables	Coupled thermomechanical FE Model	Graph theory (Deformation) model			
C-shaped part without supports	Node density (nodes/mm ³)	11.30	5.0	4.5	4.0	3.5
	Node count	3705	1540	1295	1230	1080
	MAPE (%)	Ground truth	6.30	11.11	13.31	14.89
	RMSE (μm)	Ground truth	8.81	20.79	25.29	25.05
	Computation time (s)	57.10	10.93	9.77	9.04	7.95

Table 4: Graph theory model performance for the estimation of deformation in terms of MAPE, RMSE, and computation with respect to coupled thermomechanical FE analysis for C-shaped part without supports.

Part	Description	MAPE (%)	RMSE (μm)	Computation time (s)	
				Thermo-mechanical FE	Graph theory
C-shaped part without supports	Maximum layer deformation (Figure 11(a))	6.30	8.81	57.10	10.93
	Average layer deformation (Figure 11(b))	6.09	4.83		
	Deformation at (4, 1, z) mm (Figure 11(c))	5.90	1.26		
	Deformation at (7, 1, z) mm (Figure 11(d))	3.94	0.48		

3.5 C-shaped Part with Supports

The C-shaped part with supports, Figure 6(b), was simulated using the identical boundary conditions, material properties, and the simulation parameters of the C-shaped part without supports. Similar to the C-shaped part without supports, the geometry was converted into FE mesh. The mesh consisted of 2,752 elements (3885 nodes) having a size of $0.5 \text{ mm} \times 0.5 \text{ mm} \times 0.5 \text{ mm}$.

3.5.1 Thermal History Prediction

The coupled thermomechanical FE and graph theory thermal history predictions of the average surface temperature are overlaid in Figure 12 (a). The thermal predictions at two specific locations, namely, (4 mm, 1 mm, z mm), and (17 mm, 1 mm, z mm) are also overlaid in Figure 12(b) and Figure 12(c), respectively. The error in the thermal history of the graph theory approach in comparison to the coupled thermomechanical FE solution for average surface temperature is MAPE 2% and RMSE 23°C. At location (4 mm, 1 mm, z mm) the error in comparison to the coupled thermomechanical FE model is 1% (MAPE) and 10 °C (RMSE). At the second location (17 mm, 1 mm, z mm), the error is 3% (MAPE) and 28 °C (RMSE). The graph theory thermal simulation converged in ~7 seconds while the coupled thermomechanical FE simulation in ~61 seconds.

Shown in Figure 13 is a qualitative comparison of temperature distribution on the completion of the C-shaped part with supports obtained from the coupled thermomechanical FE model, graph theory thermal model, and Netfabb.

Comparing Figure 12(a) and Figure 9(a) we note that the C-shaped part with supports depicts a more gradual decrease in surface temperature in contrast to the C-shaped part

without supports. Further, the temperature of the final layer of the C-shaped part with supports is almost 200 °C lower than its counterpart without supports.

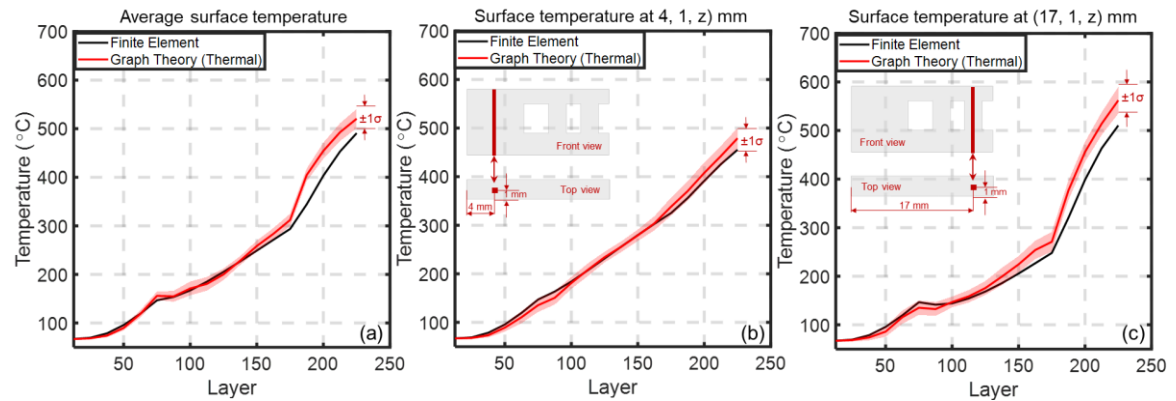


Figure 12: Thermal history of the C-shaped part with supports showing (a) average surface temperature at the end of each layer; (b) & (c) are the temperatures measured at two different coordinates for different layer heights of z (4 mm, 1 mm, z mm), and (17 mm, 1 mm, z mm), respectively.

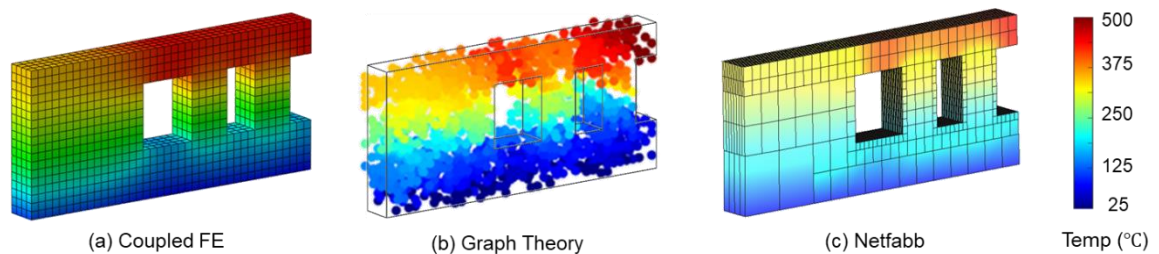


Figure 13: Qualitative comparison of the thermal history predictions at the completion of the part from (a) coupled thermomechanical FE model, (b) graph theory (Thermal) model, and (c) Netfabb.

3.5.2 Deformation Prediction

The deformation of the C-shaped part with supports was predicted using the coupled thermomechanical FE model and the graph theory (Deformation) approach at different locations. The results are depicted in Figure 14 and summarized in Table 5 and Table 6.

For the scenarios tested, the graph theory approach predicted the deformation in the z-direction with MAPE $\sim 9\%$ and $4 \mu\text{m}$ RMSE. The computation time of the graph theory (Deformation) approach was ~ 12 seconds compared to ~ 61 seconds with the coupled thermomechanical FE model.

The beneficial effects of using supports are evident in comparing Figure 14(a) and Figure 14(b), for the C-shaped part with supports alongside Figure 11(a) and Figure 11(b), respectively. The maximum and average layer deformation in the C-shaped part with supports is significantly less than $40 \mu\text{m}$. In other words, the C-shaped part with supports mitigates the tendency for a recoater crash by avoiding heat retention in the overhang region. The supports act as conduits to conduct the heat away from the overhang region. The prediction error (i.e., the MAPE and the RMSE) decreases with the increase of the node density (node per mm^3) as evident in Table 5.

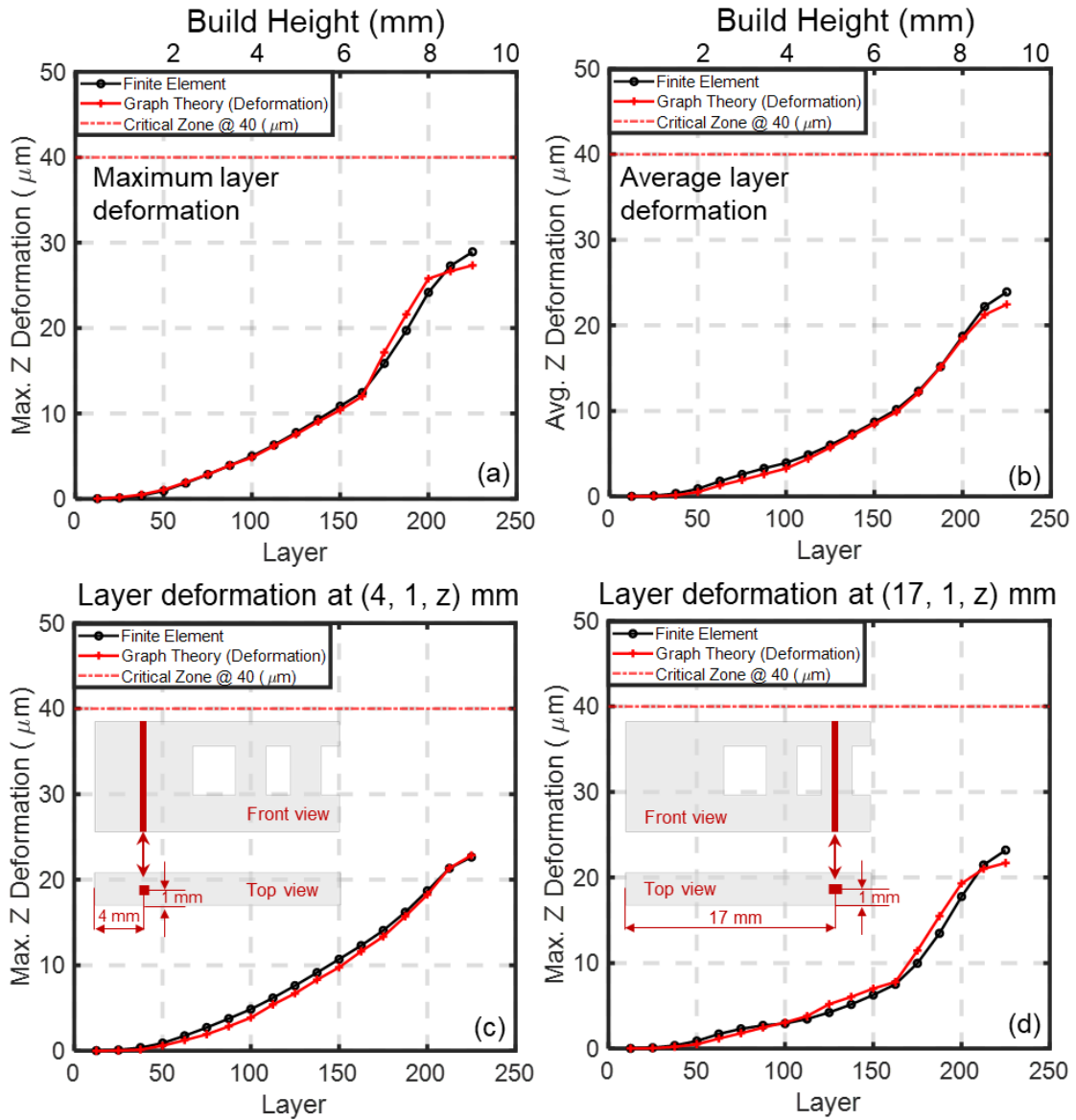


Figure 14: Comparison of deformation predictions for C-shaped part with supports between the coupled thermomechanical FE and the graph theory (Deformation) approaches.

Table 5: Graph theory (Deformation) model performance in terms of MAPE, RMSE, and computation time with respect to the coupled thermomechanical FE model. The MAPE and RMSE are estimated based on the maximum deformation of each layer.

Part	Variables	Coupled thermomechanical FE Model	Graph theory (Deformation) model			
C-shaped part with supports	Node density (nodes/mm ³)	11.30	5.0	4.5	4.0	3.5
	Node count	3885	1620	1460	1295	1140
	MAPE (%)	Ground truth	3.74	8.04	13.78	17.02
	RMSE (μm)	Ground truth	1.28	2.07	2.58	3.67
	Computation time (s)	60.70	11.56	11.10	9.83	8.59

Table 6: Graph theory model performance for the estimation of deformation in terms of MAPE, RMSE, and computation with respect to coupled thermomechanical FE analysis for C-shaped part with supports.

Part	Description	MAPE (%)	RMSE (μm)	Computation time (s)	
				Thermo-mechanical FE	Graph theory
C-shaped part with supports	Maximum layer deformation (Figure 14(a))	3.74	1.28	60.70	11.56
	Average layer deformation (Figure 14(b))	3.02	3.47		
	Deformation at (4, 1, z) mm (Figure 14(c))	8.77	0.68		
	Deformation at (17, 1, z) mm (Figure 14(d))	8.76	1.25		

CHAPTER 4 – EXPERIMENTAL VALIDATION

To validate the graph theory (Deformation) approach for predicting recoater crashes, experiments were conducted on an open architecture LPBF platform at Edison Welding Institute, Columbus, Ohio. These experiments are detailed in our previous work [90]. The schematic and pictures of the setup are shown in Figure 15; the resulting build plate is shown in Figure 15. The material was Inconel 718. The build required ~ 10 hours to complete.

The system was integrated with a thermal camera inside the chamber to acquire the surface temperature measurements of the part as it was being built. The thermal camera was inclined at 80° to the horizontal. The thermal camera (Micro Epsilon, model TIM 640) had a spectral range of 8 to 14 μm (longwave infrared spectrum), and an optical resolution of 640 pixels \times 480 pixels. The spatial resolution was ~20 pixels per mm^2 . The thermal camera was triggered to capture images of the powder bed only when the laser was actively melting a layer. The thermal camera stopped recording when the laser finished scanning a layer. In other words, the camera was turned on only when the laser was active. The thermal camera was calibrated to an absolute temperature scale using a reference thermocouple measurement as described by Yavari *et al.* [90]. Temperature measurement in LPBF is predominantly based on infrared thermography of the surface layers, as there is no practically viable approach to observe the temperature trends in the interior of an LPBF part without halting the process.

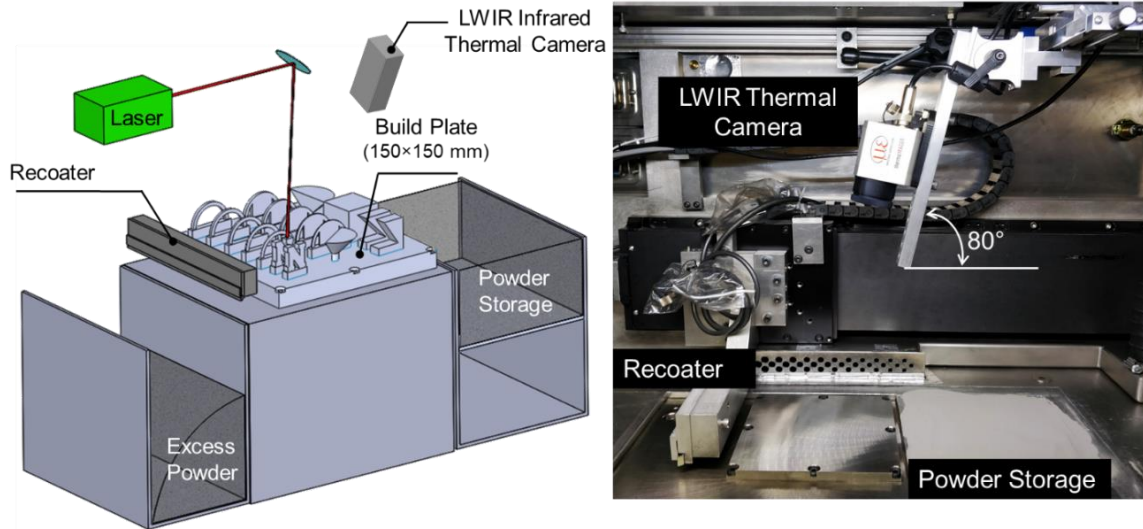


Figure 15: The schematic of the open architecture build platform and photograph of the setup. A longwave infrared thermal camera located above the build plate and inclined at 80° to the horizontal plane is used to capture the part surface temperature during the build process. Image from Yavari *et al.* [90].

The graph theory (Deformation) approach is applied to predict recoater crashes of the arch-shaped parts are shown on the build plate in Figure 2. There are two types of arch-shaped parts, namely, arches built with supports and those without supports. These parts are analogous to the C-shaped parts with and without supports studied in Chapter 3.

As shown in Figure 16, all the arches have the same length of 40 mm and height of 26 mm, and base width of 5 mm but have varying gauge thicknesses (t) from 0.5 mm to 2.5 mm in steps of 0.5 mm. As evident from Figure 2, all the arches without supports, except the arch with gauge thickness $t = 1.5$ mm, failed during printing due to recoater crash. The arches are labeled per their gauge thickness, as follows: the arch with thickness $t = 0.5$ mm is labeled as A05; $t = 1.0$ mm as A10; $t = 1.5$ mm as A15; and so on. The arches with supports are labeled as SA05, SA10, and so on.

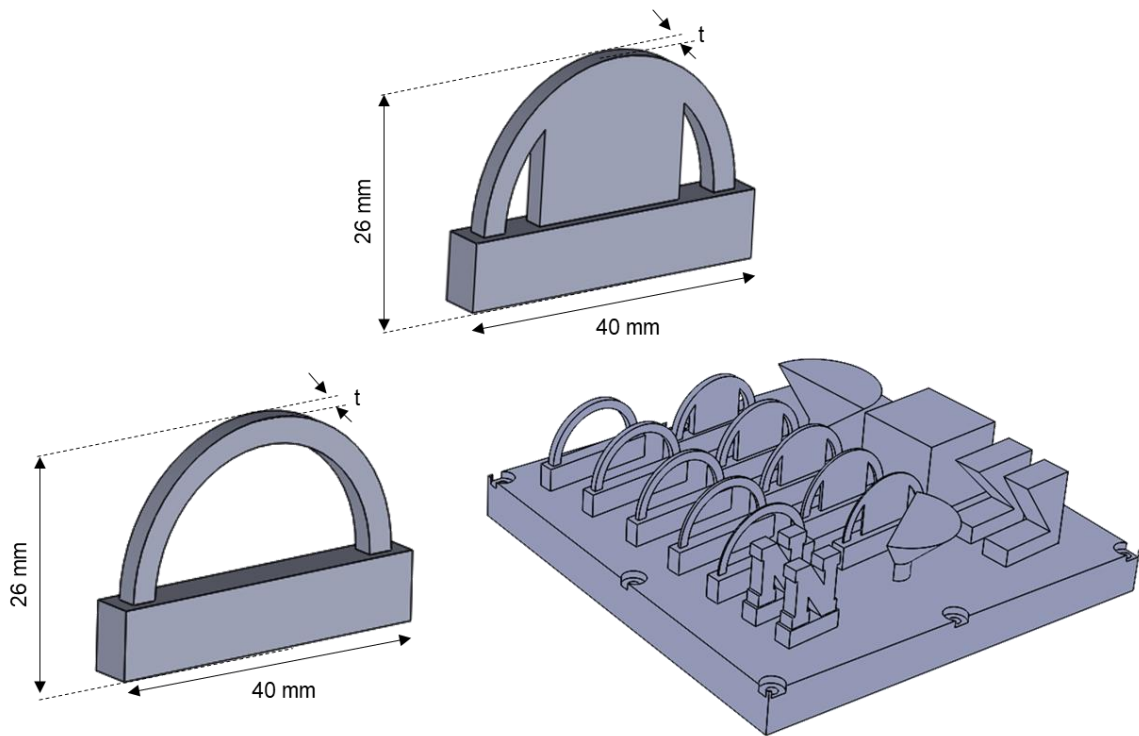


Figure 16: Arch-Shaped geometries (with/without supports) with varying gauge thicknesses, $t = 0.5, 1.0, 1.5, 2.0,$ and 2.5 mm.

The arches A05 and A10 had recoater crashes at layer 556 and 548, respectively, corresponding to the build height of 22 mm; arches A20 and A25 crashed at a build height of 23 mm corresponding to layer 574. Arch A15 did not experience a recoater crash as it was protected by neighboring arches. To explain further, the superelevation of the arches on either side of A15 (A10 and A20) lifted the recoater blade and created sufficient clearance to prevent contact with the part. Representative thermal camera frames corresponding to the layers where the unsupported arches underwent recoater crashes are shown in Figure 17.

These recoater crash events are evident from the infrared thermal image. After the recoater crash event of arch A10 at layer 548, higher thermal intensity is recorded in its location compared to the rest of the arches at that same layer. To explain further, following the

breakage of the arch A10 due to the recoater crash, the laser scans an area of the powder bed without a solid part underneath. Since compared to a solid part, powder is a poor conductor of heat, the temperature of the powder bed increases. The same heat retention phenomena are also evident with the recoater crashes of the arches A05, A20, and A25 corresponding to layers 556 and 574. Indeed, the debris from arch A10 is observed at layer 574 in the thermal image, nearly 25 layers after the recoater crash.

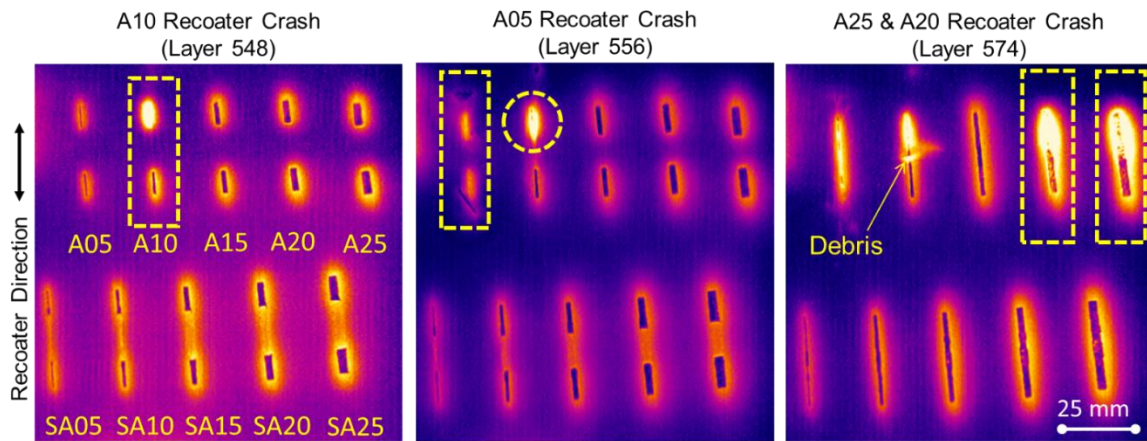


Figure 17: IR camera images of recoater crash incidents at layers 548, 556, and 574 corresponding to arches A10, A05, and A25 & A20. Note that the relative intensity of the failed arches is higher compared to the other arches which indicate relatively higher heat retention occurring following the recoater interference with these arches. The debris of the crashed arch A10 is still evident in the subsequent layers. Image from Yavari *et al.* [90].

Ten arches (five arches with supports and five arches without supports) were simulated (one at a time). For brevity, the results of four representative arches A10, A20, A25, and SA25 are reported. The boundary conditions, material properties, and simulation parameters are reported in Table 1. The corresponding arch thickness, number of solid mesh elements, and nodes are shown in Table 7. Each arch contained 52 superlayers corresponding to 650 actual layers; each super layer corresponded to 12.5 actual layers equating to 0.5 mm. The super layer thickness was identically implemented in coupled thermomechanical FE and graph theory approaches.

Table 7: Part properties of arches showing gauge thickness, number of mesh elements, and nodes in each arch.

Part	Gauge thickness (t) (mm)	Part Label	Number of FE mesh element	Number of nodes in graph theory
Arches without supports	1.0	A10	17,576	1,920
	2.0	A20	20,932	2,155
	2.5	A25	23,611	2,260
Arches with supports	2.5	SA25	26,554	2,635

4.1 Prediction of Thermal History

In Figure 18, the surface temperature at the end of a layer is predicted using the graph theory, and results from the coupled thermomechanical FE models are overlaid on the experimental data. It is observed that both the graph theory thermal model and coupled thermomechanical FE model closely track the experimental thermal observation up to the point of the recoater crash. The thermal prediction results are summarized in Table 8.

A qualitative comparison of the thermal prediction of two types of arches – arch without supports (A25), and arch with supports (SA25) – at three different build heights is shown in Figure 19. The thermal fields of the coupled thermomechanical FE, graph theory (Thermal), and Netfabb models show that the arch without supports (A25) is accumulating heat as it builds up. At one point, the heat retention caused enough deformation in the build direction to interfere with the recoater which ultimately caused the recoater crash. Meanwhile, the arch with supports (SA25) created a conductive path between the thin legs and the base that prevented heat accumulation. As a result, heat-induced deformation is relatively low and no subsequent recoater crash occurred.

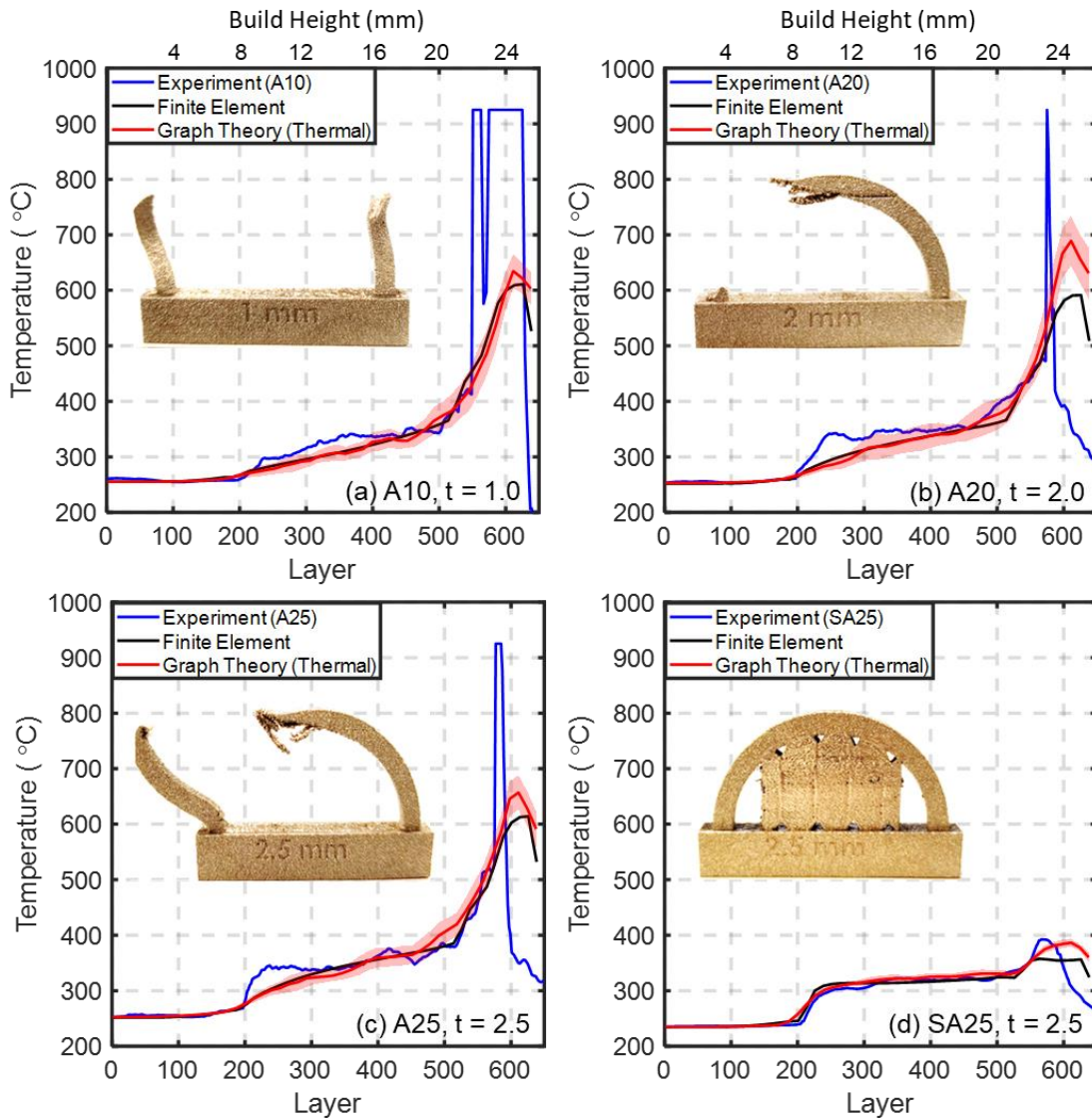


Figure 18: The surface temperature observed during experiments (blue line) overlaid on the coupled thermomechanical FE model (black), and graph theory (red) thermal history predictions for four representative arches (a) A10, (b) A20, (c) A25, and (d) SA25.

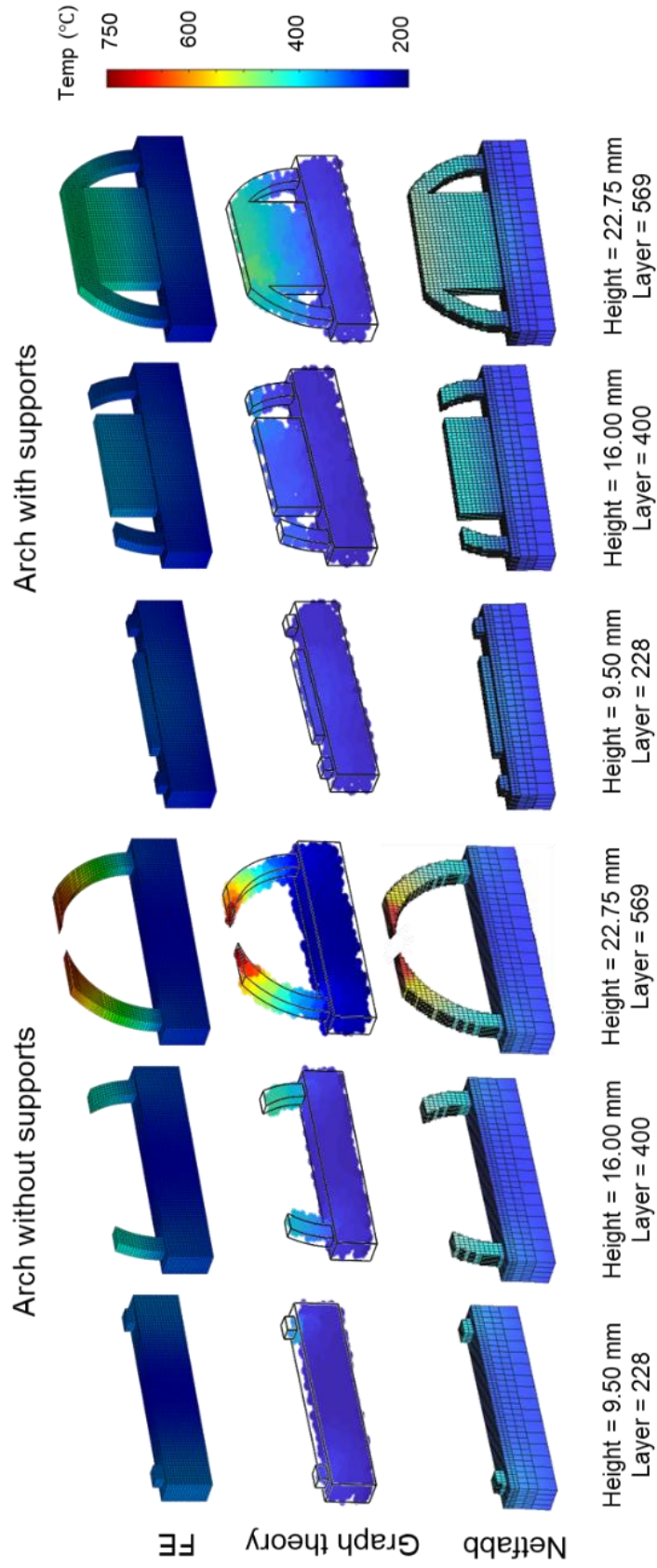


Figure 19: Qualitative comparison of the thermal history predictions for arches 2.5 mm with (SA25) and without (A25) supports at the completion of three different build heights from coupled thermomechanical FE model, graph theory (Thermal), and Netfabb.

Table 8: Coupled thermomechanical FE and graph theory thermal model performance for the estimation of thermal history in terms of MAPE, RMSE, and computation, with respect to experimental data.

Part	MAPE - before the first crash (Layer 548) (%)		RMSE- before the first crash (°C)		Computation Time (s)	
	Coupled FE	Graph theory	Coupled FE	Graph theory	Coupled FE	Graph theory
A10 (Figure 18(a))	4.40	3.66	19.85	15.40	1523	193
A20 (Figure 18(b))	5.80	3.98	29.05	20.12	1601	214
A25 (Figure 18(c))	4.19	3.57	26.63	18.32	1683	224
SA25 (Figure 18(d))	2.13	2.03	12.99	8.82	1716	273

4.2 Prediction of Recoater Crash

Deformation predictions from the coupled thermomechanical FE, graph theory (Deformation), and Netfabb models are shown in Figure 20 and reported in Table 9 and Table 10. The qualitative comparison of deformation predictions from the coupled thermomechanical FE, graph theory (Deformation), and Netfabb approaches is shown in Figure 21. As is evident, the arches without supports (A10, A20, and A25 in Figure 20(a), Figure 20(b), and Figure 20(c)) deform considerably. When the part reaches nearly 23 mm in height, the deformation becomes sufficient to exceed the recoater clearance of 40 μm , increasing the likelihood of a recoater crash. Meanwhile, the arch with supports, SA25 shows the deformation in the vertical build direction remains below 40 μm as the supports

create a conductive path to prevent heat retention. Hence, a recoater crash is unlikely to occur for SA25.

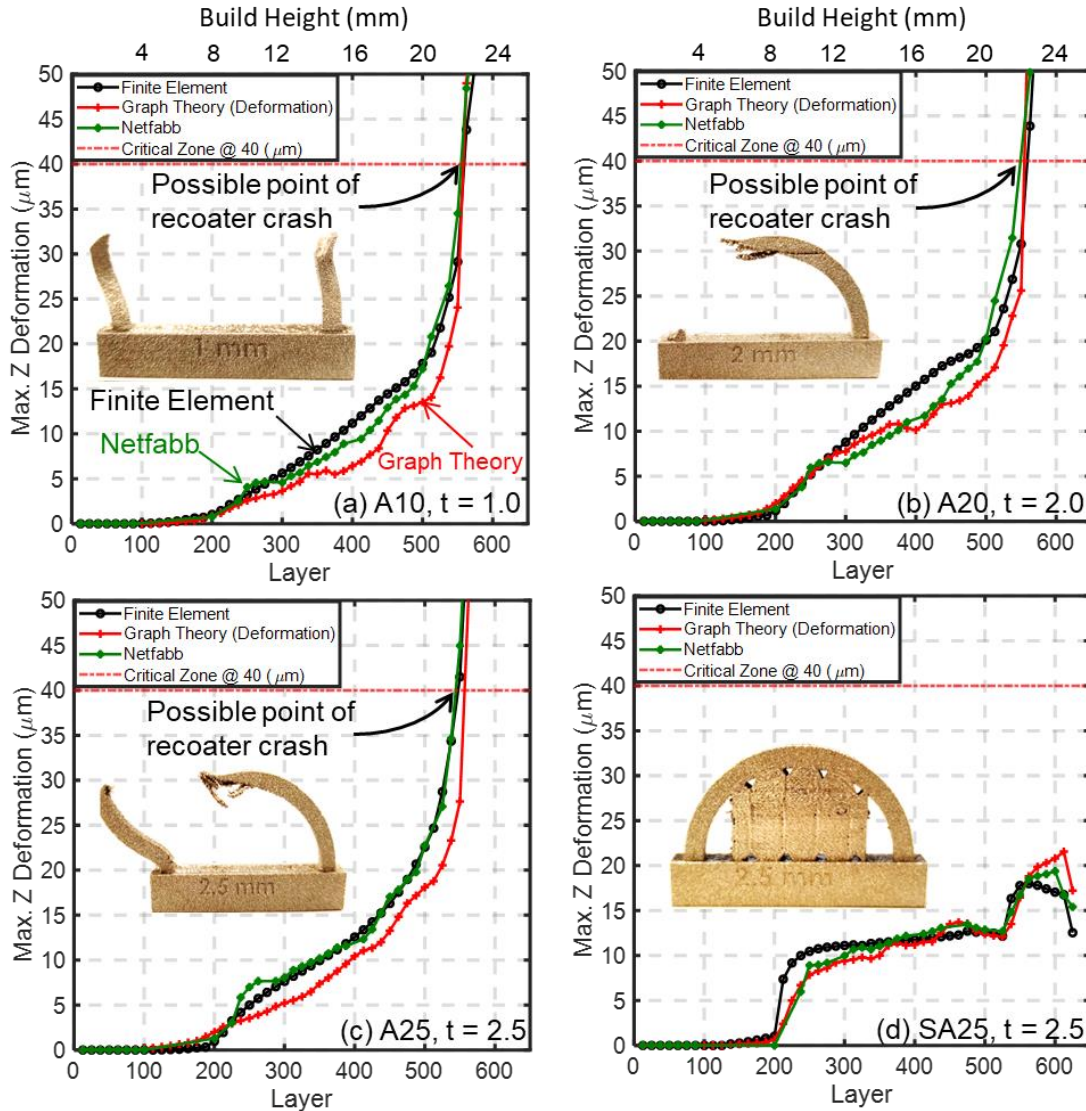


Figure 20: Deformation predictions of each layer using coupled thermomechanical FE (black), graph theory-based (red), and Netfabb (green) models corresponding to the arches (a) A10, (b) A20, (c) A25, and (d) SA25. The recoater crash occurs when deformation exceeds the layer height of $40 \mu\text{m}$ (red dotted).

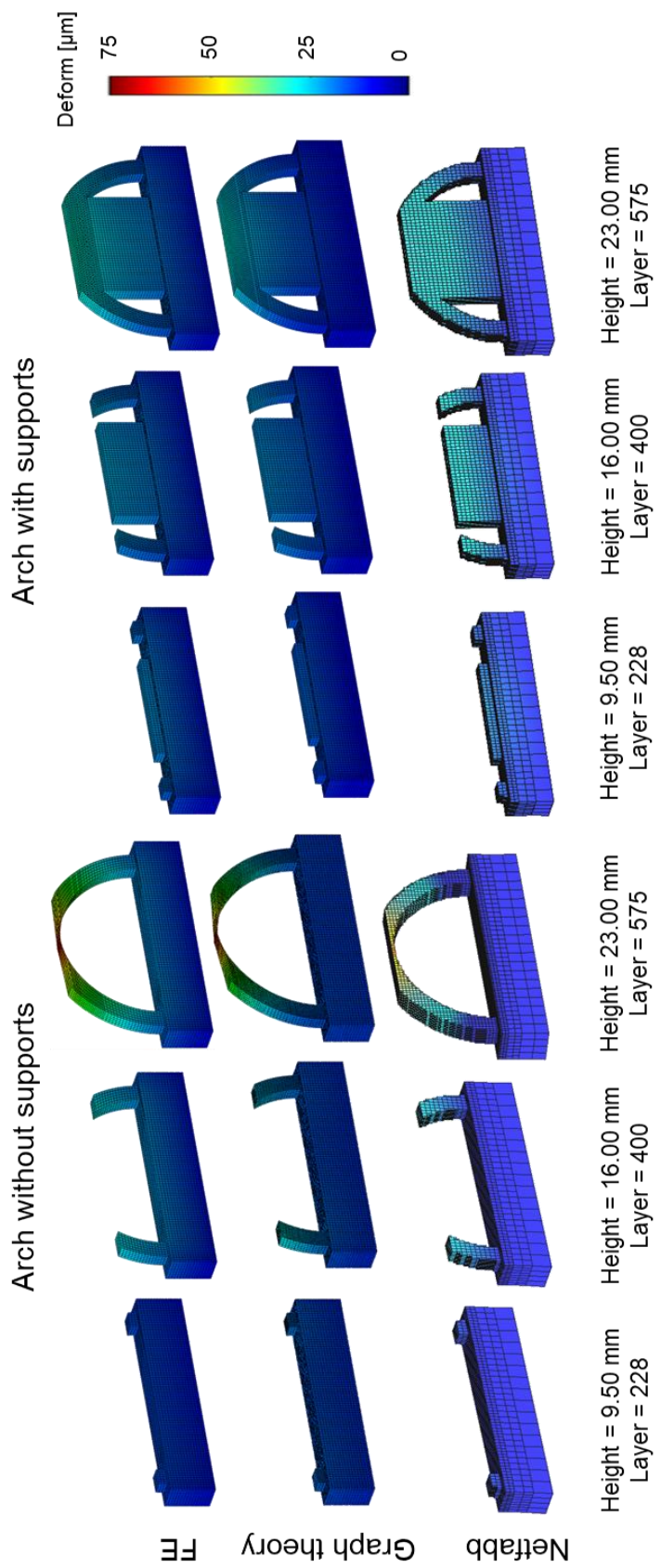


Figure 21: Qualitative comparison of the deformation predictions at three different build heights using coupled thermomechanical FE, graph theory (Deformation), and Netfabb models of the arch without supports A25 and arch with supports SA25.

In Table 9, the layer at which a recoater crash is likely to occur is predicted using graph theory (Deformation), and the results are compared with those from coupled thermomechanical FE and Netfabb. We note that a recoater crash is likely to occur when the maximum deformation of the top surface of the part exceeds 40 μm (the layer thickness). The graph theory (Deformation) approach correctly predicts the moment of the recoater crash for all the unsupported arches, as well as correctly anticipates that a recoater crash is unlikely to occur for the supported arches. The graph (Deformation) approach predicts that a recoater crash would occur about 12 layers before the recoater crash is observed in the experiment in the unsupported arches except for the case of the arch A10. Similar results are reported by both the coupled thermomechanical FE and Netfabb models.

Table 9: Summary of experimental recoater crash, and the recoater crash predictions obtained from coupled thermomechanical FE, graph theory (Deformation), and Netfabb approaches, respectively. The number in the parentheses is the computation time in seconds.

Part	Layer at which recoater crash occurred in the experiment	Layer of recoater crash prediction		
		Coupled thermomechanical FE	Graph theory (Deformation)	Netfabb
A05	556	538 (1512)	550 (189)	550 (207)
A10	548	562 (1523)	562 (193)	560 (229)
A15	No crash	562 (1536)	562 (211)	550 (239)
A20	574	562 (1601)	562 (214)	560 (246)
A25	574	550 (1683)	562 (224)	550 (252)
SA25, and all supported arches	No crash	No crash (1716)	No crash (273)	No crash (351)

Table 10: Summary of Node density, Node count, Mean Percentage Error (MAPE), Root Mean Square Error (RMSE), and computation time for the coupled thermomechanical FE model, graph theory (Deformation), and Netfabb simulations.

Part	Variables	Coupled thermomechanical FE	Graph theory (Deformation)	Netfabb
A05	Node count	19930	1795	16668
	MAPE (%)	Ground truth	13.79	12.61
	RMSE (μm)	Ground truth	2.54	3.34
	Computation time (s)	1512	189	207
A10	Node count	21588	1920	24370
	MAPE (%)	Ground truth	18.8	9.80
	RMSE (μm)	Ground truth	2.90	2.30
	Computation time (s)	1523	193	229
A15	Node count	23348	2035	26764
	MAPE (%)	Ground truth	18.28	10.29
	RMSE (μm)	Ground truth	2.78	3.77
	Computation time (s)	1536	211	239
A20	Node count	25123	2155	30686
	MAPE (%)	Ground truth	13.00	10.80
	RMSE (μm)	Ground truth	2.60	2.20
	Computation time (s)	1601	214	246
A25	Node count	26678	2260	24896
	MAPE (%)	Ground truth	15.40	13.00
	RMSE (μm)	Ground truth	3.90	3.20
	Computation time (s)	1683	224	252
SA25	Node count	26964	2635	40323
	MAPE (%)	Ground truth	8.40	5.27
	RMSE (μm)	Ground truth	1.60	1.09
	Computation time (s)	1716	273	351

CHAPTER 5 – CONCLUSIONS AND FUTURE WORK

This work presented a novel graph theory-based approach for thermomechanical modeling in the Laser Powder Bed Fusion (LPBF) process. The approach was developed by combining a meshfree graph theory thermal model with an FE-based mechanical model. The approach is applied for predicting a particular type of commonly occurring thermal-induced deformation failure in LPBF called recoater crash. The advantage of this approach is its computational efficiency when compared to a coupled thermomechanical FE model. The specific contributions of this work are as follows:

1. Two LPBF test parts were simulated using the graph theory approach. The deformation in the vertical direction was predicted using the graph theory (Deformation) approach and the predictions were compared with the coupled thermomechanical FE analysis which was considered as the ground truth. It was found that the deformation predictions obtained from the graph theory (Deformation) approach closely agreed with the coupled thermomechanical FE solutions. The calculated errors were less than 10% (MAPE), and 10 μm (RMSE). The key result is that the graph theory (Deformation) approach converges about 5 times faster than the coupled thermomechanical FE approach.
2. The experimental validation was carried out on an open architecture LPBF platform at Edison Welding Institute, Columbus, Ohio. Ten arch-shaped parts encompassing different gauge thicknesses were built. Two types of arches were built, namely, arches with supports and arches without supports. All the arches without supports except arch A15 experienced recoater crash during the experiment, while all five arches with supports were successfully printed without

the occurrence of recoater crash. The graph theory (Deformation) approach predicted the likelihood of a recoater crash for all the arches without supports. The results agreed with both the coupled thermomechanical FE model results and that of a commercial FE-based LPBF simulation software (Autodesk Netfabb). The graph theory (Deformation) approach converged approximately 6 times faster than the coupled thermomechanical FE approach (5 minutes vs 30 minutes).

In summary, this research develops and applies a computationally efficient graph theory-based approach for part-level thermomechanical modeling to predict thermal-induced deformation, specifically, in LPBF. The approach is applied to predictions of recoater crashes. The approach is valuable to LPBF practitioners. The following questions are yet to be addressed which we will endeavor to answer in our forthcoming works:

1. What is the effect of the thermal history on residual stress?
2. How much would the part distort when removed from the build plate?
3. What is the effect of thermal-induced deformation on the geometric aspects, such as causality, planarity, straightness, etc.?
4. What is the likelihood of supports failure?

The graph theory (Deformation) approach drastically reduces the time required for predicting deformation and recoater crashes. As a consequence, a user can identify and rapidly correct red flag problems in the part design and processing conditions before the part is printed. This work presents an opportunity to evolve from a build-and-lost (trial and error) procedure to a physics-based strategy for process optimization in LPBF, thus leading to accelerating time-to-market for LPBF parts.

REFERENCES CITED

- [1] Schmidt, M., Merklein, M., Bourell, D., Dimitrov, D., Hausotte, T., Wegener, K., Overmeyer, L., Vollertsen, F., and Levy, G. N., 2017, "Laser based additive manufacturing in industry and academia," *CIRP Annals*, 66(2), pp. 561-583. doi: <https://doi.org/10.1016/j.cirp.2017.05.011>
- [2] Tofail, S. A. M., Koumoulos, E. P., Bandyopadhyay, A., Bose, S., O'Donoghue, L., and Charitidis, C., 2018, "Additive manufacturing: scientific and technological challenges, market uptake and opportunities," *Materials Today*, 21(1), pp. 22-37. doi: <https://doi.org/10.1016/j.mattod.2017.07.001>
- [3] Bourell, D. L., 2016, "Perspectives on Additive Manufacturing," *Annual Review of Materials Research*, 46(1), pp. 1-18. doi: 10.1146/annurev-matsci-070115-031606
- [4] Milewski, J. O., 2017, "Additive manufacturing of metals," *From Fundamental Technology to Rocket Nozzles, Medical Implants, and Custom Jewelry*, Springer. doi:
- [5] Kellner, T., 2018, "Fired Up: GE Successfully Tested Its Advanced Turboprop Engine With 3D-Printed Parts," *GE reports*.doi:
- [6] Yavari, R., Williams, R., Riensche, A., Hooper, P. A., Cole, K. D., Jacquemetton, L., Halliday, H., and Rao, P. K., 2021, "Thermal modeling in metal additive manufacturing using graph theory – Application to laser powder bed fusion of a large volume impeller," *Additive Manufacturing*, 41, p. 101956. doi: <https://doi.org/10.1016/j.addma.2021.101956>
- [7] DebRoy, T., Wei, H., Zuback, J., Mukherjee, T., Elmer, J., Milewski, J., Beese, A., Wilson-Heid, A., De, A., and Zhang, W., 2018, "Additive manufacturing of metallic components—process, structure and properties," *Progress in Materials Science*, 92, pp. 112-224. doi:
- [8] Gorelik, M., 2017, "Additive manufacturing in the context of structural integrity," *International Journal of Fatigue*, 94, pp. 168-177. doi: <https://doi.org/10.1016/j.ijfatigue.2016.07.005>
- [9] Uriondo, A., Esperon-Miguez, M., and Perinpanayagam, S., 2015, "The present and future of additive manufacturing in the aerospace sector: A review of important aspects," *Proceedings of the Institution of Mechanical Engineers, Part G: Journal of Aerospace Engineering*, 229(11), pp. 2132-2147. doi: 10.1177/0954410014568797
- [10] Sames, W. J., List, F., Pannala, S., Dehoff, R. R., and Babu, S. S., 2016, "The metallurgy and processing science of metal additive manufacturing," *International Materials Reviews*, 61(5), pp. 315-360. doi:
- [11] Seifi, M., Salem, A., Beuth, J., Harrysson, O., and Lewandowski, J. J., 2016, "Overview of materials qualification needs for metal additive manufacturing," *Jom*, 68(3), pp. 747-764. doi:
- [12] Gorelik, M., "Additive manufacturing and risk mitigation—a regulatory perspective," *Proc. FAA-AF Additive Manufacturing Workshop, Dayton, OH, USA*. In: DOT/FAA/TC-16/15.
- [13] Seifi, M., Gorelik, M., Waller, J., Hrabe, N., Shamsaei, N., Daniewicz, S., and Lewandowski, J. J., 2017, "Progress Towards Metal Additive Manufacturing

- Standardization to Support Qualification and Certification," *JOM*, 69(3), pp. 439-455. doi: 10.1007/s11837-017-2265-2
- [14] Bourell, D., Kruth, J. P., Leu, M., Levy, G., Rosen, D., Beese, A. M., and Clare, A., 2017, "Materials for additive manufacturing," *CIRP Annals*, 66(2), pp. 659-681. doi: <https://doi.org/10.1016/j.cirp.2017.05.009>
- [15] Thomas-Seale, L. E. J., Kirkman-Brown, J. C., Attallah, M. M., Espino, D. M., and Shepherd, D. E. T., 2018, "The barriers to the progression of additive manufacture: Perspectives from UK industry," *International Journal of Production Economics*, 198, pp. 104-118. doi: <https://doi.org/10.1016/j.ijpe.2018.02.003>
- [16] Bandyopadhyay, A., and Traxel, K. D., 2018, "Invited review article: Metal-additive manufacturing—Modeling strategies for application-optimized designs," *Additive Manufacturing*, 22, pp. 758-774. doi: <https://doi.org/10.1016/j.addma.2018.06.024>
- [17] Martin, A. A., Calta, N. P., Khairallah, S. A., Wang, J., Depond, P. J., Fong, A. Y., Thampy, V., Guss, G. M., Kiss, A. M., Stone, K. H., Tassone, C. J., Nelson Weker, J., Toney, M. F., van Buuren, T., and Matthews, M. J., 2019, "Dynamics of pore formation during laser powder bed fusion additive manufacturing," *Nature Communications*, 10(1), p. 1987. doi: 10.1038/s41467-019-10009-2
- [18] Francois, M. M., Sun, A., King, W. E., Henson, N. J., Turret, D., Bronkhorst, C. A., Carlson, N. N., Newman, C. K., Haut, T., Bakosi, J., Gibbs, J. W., Livescu, V., Vander Wiel, S. A., Clarke, A. J., Schraad, M. W., Blacker, T., Lim, H., Rodgers, T., Owen, S., Abdeljawad, F., Madison, J., Anderson, A. T., Fattebert, J. L., Ferencz, R. M., Hodge, N. E., Khairallah, S. A., and Walton, O., 2017, "Modeling of additive manufacturing processes for metals: Challenges and opportunities," *Current Opinion in Solid State and Materials Science*, 21(4), pp. 198-206. doi: <https://doi.org/10.1016/j.cossms.2016.12.001>
- [19] Khairallah, S. A., Anderson, A. T., Rubenchik, A., and King, W. E., 2016, "Laser powder-bed fusion additive manufacturing: Physics of complex melt flow and formation mechanisms of pores, spatter, and denudation zones," *Acta Materialia*, 108, pp. 36-45. doi: 10.1016/j.actamat.2016.02.014
- [20] King, W., Anderson, A., Ferencz, R., Hodge, N., Kamath, C., and Khairallah, S., 2014, "Overview of modelling and simulation of metal powder-bed fusion process at Lawrence Livermore National Laboratory," *Materials Science and Technology*, 31(8), pp. 957-968. doi:
- [21] Dovgyy, B., Piglione, A., Hooper, P. A., and Pham, M.-S., 2020, "Comprehensive assessment of the printability of CoNiCrFeMn in Laser Powder Bed Fusion," *Materials & Design*, 194, p. 108845. doi: <https://doi.org/10.1016/j.matdes.2020.108845>
- [22] Gouge, M., Michaleris, P., Denlinger, E., and Irwin, J., 2018, "Chapter 2 - The Finite Element Method for the Thermo-Mechanical Modeling of Additive Manufacturing Processes," *Thermo-Mechanical Modeling of Additive Manufacturing*, M. Gouge, and P. Michaleris, eds., Butterworth-Heinemann, pp. 19-38. doi: <https://doi.org/10.1016/B978-0-12-811820-7.00003-3>
- [23] de Saracibar, C. A., Lundbäck, A., Chiumenti, M., and Cervera, M., 2014, "Shaped metal deposition processes," *Encyclopedia of thermal stresses*, pp. 4346-4355. doi:

- [24] Oliveira, J. P., Santos, T. G., and Miranda, R. M., 2020, "Revisiting fundamental welding concepts to improve additive manufacturing: From theory to practice," *Progress in Materials Science*, 107, p. 100590. doi: <https://doi.org/10.1016/j.pmatsci.2019.100590>
- [25] Hibbitt, H. D., and Marcal, P. V., 1973, "A numerical, thermo-mechanical model for the welding and subsequent loading of a fabricated structure," *Computers & Structures*, 3(5), pp. 1145-1174. doi: [https://doi.org/10.1016/0045-7949\(73\)90043-6](https://doi.org/10.1016/0045-7949(73)90043-6)
- [26] Friedman, E., 1975, "Thermomechanical Analysis of the Welding Process Using the Finite Element Method," *Journal of Pressure Vessel Technology*, 97(3), pp. 206-213. doi: 10.1115/1.3454296
- [27] Argyris, J. H., Szimmat, J., and Willam, K. J., 1982, "Computational aspects of welding stress analysis," *Computer Methods in Applied Mechanics and Engineering*, 33(1), pp. 635-665. doi: [https://doi.org/10.1016/0045-7825\(82\)90126-8](https://doi.org/10.1016/0045-7825(82)90126-8)
- [28] Tekriwal, P., and Mazumder, J., 1988, "Finite element analysis of three-dimensional transient heat transfer in GMA Welding, AWS Welding J," *Res. Suppl*, 67. doi:
- [29] Free, J. A., and Porter Goff, R. F. D., 1989, "Predicting residual stresses in multi-pass weldments with the finite element method," *Computers & Structures*, 32(2), pp. 365-378. doi: [https://doi.org/10.1016/0045-7949\(89\)90048-5](https://doi.org/10.1016/0045-7949(89)90048-5)
- [30] Li, Y., Zhou, K., Tan, P., Tor, S. B., Chua, C. K., and Leong, K. F., 2018, "Modeling temperature and residual stress fields in selective laser melting," *International Journal of Mechanical Sciences*, 136, pp. 24-35. doi: <https://doi.org/10.1016/j.ijmecsci.2017.12.001>
- [31] Bayat, M., Klingaa, C. G., Mohanty, S., De Baere, D., Thorborg, J., Tiedje, N. S., and Hattel, J. H., 2020, "Part-scale thermo-mechanical modelling of distortions in Laser Powder Bed Fusion – Analysis of the sequential flash heating method with experimental validation," *Additive Manufacturing*, 36, p. 101508. doi: <https://doi.org/10.1016/j.addma.2020.101508>
- [32] Yu, T., Li, M., Breaux, A., Atri, M., Obeidat, S., and Ma, C., 2019, "Experimental and numerical study on residual stress and geometric distortion in powder bed fusion process," *Journal of Manufacturing Processes*, 46, pp. 214-224. doi: <https://doi.org/10.1016/j.jmapro.2019.09.010>
- [33] Ma, C., Vadali, M., Duffie, N. A., Pfefferkorn, F. E., and Li, X., 2013, "Melt pool flow and surface evolution during pulsed laser micro polishing of Ti6Al4V," *Journal of Manufacturing Science and Engineering*, 135(6). doi:
- [34] Alimardani, M., Toyserkani, E., and Huissoon, J. P., 2007, "A 3D dynamic numerical approach for temperature and thermal stress distributions in multilayer laser solid freeform fabrication process," *Optics and Lasers in Engineering*, 45(12), pp. 1115-1130. doi: <https://doi.org/10.1016/j.optlaseng.2007.06.010>
- [35] Gu, D., and He, B., 2016, "Finite element simulation and experimental investigation of residual stresses in selective laser melted Ti–Ni shape memory alloy," *Computational Materials Science*, 117, pp. 221-232. doi: <https://doi.org/10.1016/j.commatsci.2016.01.044>
- [36] Dai, K., and Shaw, L., 2004, "Thermal and mechanical finite element modeling of laser forming from metal and ceramic powders," *Acta Materialia*, 52(1), pp. 69-80. doi: <https://doi.org/10.1016/j.actamat.2003.08.028>

- [37] Li, C., Fu, C. H., Guo, Y. B., and Fang, F. Z., 2016, "A multiscale modeling approach for fast prediction of part distortion in selective laser melting," *Journal of Materials Processing Technology*, 229, pp. 703-712. doi: <https://doi.org/10.1016/j.jmatprotec.2015.10.022>
- [38] Chin, R. K., Beuth, J. L., and Amon, C. H., 1996, "Thermomechanical modeling of molten metal droplet solidification applied to layered manufacturing," *Mechanics of Materials*, 24(4), pp. 257-271. doi: [https://doi.org/10.1016/S0167-6636\(96\)00037-3](https://doi.org/10.1016/S0167-6636(96)00037-3)
- [39] Song, X., Xie, M., Hofmann, F., Illston, T., Connolley, T., Reinhard, C., Atwood, R. C., Connor, L., Drakopoulos, M., Frampton, L., and Korsunsky, A. M., 2015, "Residual stresses and microstructure in Powder Bed Direct Laser Deposition (PB DLD) samples," *International Journal of Material Forming*, 8(2), pp. 245-254. doi: 10.1007/s12289-014-1163-1
- [40] Parry, L., Ashcroft, I. A., and Wildman, R. D., 2016, "Understanding the effect of laser scan strategy on residual stress in selective laser melting through thermo-mechanical simulation," *Additive Manufacturing*, 12, pp. 1-15. doi: <https://doi.org/10.1016/j.addma.2016.05.014>
- [41] Tan, P., Shen, F., Li, B., and Zhou, K., 2019, "A thermo-metallurgical-mechanical model for selective laser melting of Ti6Al4V," *Materials & Design*, 168, p. 107642. doi: <https://doi.org/10.1016/j.matdes.2019.107642>
- [42] Denlinger, E., Gouge, M., Irwin, J., and Michaleris, P., 2017, "Thermomechanical model development and in situ experimental validation of the Laser Powder-Bed Fusion Process. *Add Manuf* 16: 73–80."doi:
- [43] Li, C., Guo, Y., Fang, X., and Fang, F., 2018, "A scalable predictive model and validation for residual stress and distortion in selective laser melting," *CIRP Annals*, 67(1), pp. 249-252. doi: <https://doi.org/10.1016/j.cirp.2018.04.105>
- [44] Chen, C., Yin, J., Zhu, H., Xiao, Z., Zhang, L., and Zeng, X., 2019, "Effect of overlap rate and pattern on residual stress in selective laser melting," *International Journal of Machine Tools and Manufacture*, 145, p. 103433. doi: <https://doi.org/10.1016/j.ijmachtools.2019.103433>
- [45] Nickel, A. H., Barnett, D. M., and Prinz, F. B., 2001, "Thermal stresses and deposition patterns in layered manufacturing," *Materials Science and Engineering: A*, 317(1), pp. 59-64. doi: [https://doi.org/10.1016/S0921-5093\(01\)01179-0](https://doi.org/10.1016/S0921-5093(01)01179-0)
- [46] Chiumenti, M., Neiva, E., Salsi, E., Cervera, M., Badia, S., Moya, J., Chen, Z., Lee, C., and Davies, C., 2017, "Numerical modelling and experimental validation in Selective Laser Melting," *Additive Manufacturing*, 18, pp. 171-185. doi: <https://doi.org/10.1016/j.addma.2017.09.002>
- [47] Zaeh, M. F., and Branner, G., 2010, "Investigations on residual stresses and deformations in selective laser melting," *Production Engineering*, 4(1), pp. 35-45. doi: 10.1007/s11740-009-0192-y
- [48] Liang, X., Hayduke, D., and To, A. C., 2021, "An enhanced layer lumping method for accelerating simulation of metal components produced by laser powder bed fusion," *Additive Manufacturing*, 39, p. 101881. doi: <https://doi.org/10.1016/j.addma.2021.101881>

- [49] Williams, R. J., Davies, C. M., and Hooper, P. A., 2018, "A pragmatic part scale model for residual stress and distortion prediction in powder bed fusion," *Additive Manufacturing*, 22, pp. 416-425. doi: <https://doi.org/10.1016/j.addma.2018.05.038>
- [50] Bartlett, J. L., and Li, X., 2019, "An overview of residual stresses in metal powder bed fusion," *Additive Manufacturing*, 27, pp. 131-149. doi: <https://doi.org/10.1016/j.addma.2019.02.020>
- [51] Gouge, M., Denlinger, E., Irwin, J., Li, C., and Michaleris, P., 2019, "Experimental validation of thermo-mechanical part-scale modeling for laser powder bed fusion processes," *Additive Manufacturing*, 29, p. 100771. doi: <https://doi.org/10.1016/j.addma.2019.06.022>
- [52] Gouge, M., and Michaleris, P., 2018, "Thermo-Mechanical Modeling of Additive Manufacturing," Elsevier, Cambridge, MA., doi:
- [53] Gouge, M., and Michaleris, P., 2018, "Chapter 1 - An Introduction to Additive Manufacturing Processes and Their Modeling Challenges," *Thermo-Mechanical Modeling of Additive Manufacturing*, M. Gouge, and P. Michaleris, eds., Butterworth-Heinemann, pp. 3-18. doi: <https://doi.org/10.1016/B978-0-12-811820-7.00002-1>
- [54] Luo, Z., and Zhao, Y., 2018, "A survey of finite element analysis of temperature and thermal stress fields in powder bed fusion Additive Manufacturing," *Additive Manufacturing*, 21, pp. 318-332. doi: 10.1016/j.addma.2018.03.022
- [55] DebRoy, T., Wei, H. L., Zuback, J. S., Mukherjee, T., Elmer, J. W., Milewski, J. O., Beese, A. M., Wilson-Heid, A., De, A., and Zhang, W., 2018, "Additive manufacturing of metallic components – Process, structure and properties," *Progress in Materials Science*, 92, pp. 112-224. doi: <https://doi.org/10.1016/j.pmatsci.2017.10.001>
- [56] Yavari, M. R., Cole, K. D., and Rao, P., 2019, "Thermal Modeling in Metal Additive Manufacturing Using Graph Theory," *Journal of Manufacturing Science and Engineering*, 141(7). doi: 10.1115/1.4043648
- [57] Peter, N., Pitts, Z., Thompson, S., and Saharan, A., 2020, "Benchmarking build simulation software for laser powder bed fusion of metals," *Additive Manufacturing*, 36, p. 101531. doi: <https://doi.org/10.1016/j.addma.2020.101531>
- [58] Michaleris, P., 2014, "Modeling metal deposition in heat transfer analyses of additive manufacturing processes," *Finite Elements in Analysis and Design*, 86, pp. 51-60. doi: <https://doi.org/10.1016/j.finel.2014.04.003>
- [59] Francois, M. M., Sun, A., King, W. E., Henson, N. J., Turret, D., Bronkhorst, C. A., Carlson, N. N., Newman, C. K., Haut, T. S., Bakosi, J., Gibbs, J. W., Livescu, V., Vander Wiel, S. A., Clarke, A. J., Schraad, M. W., Blacker, T., Lim, H., Rodgers, T., Owen, S., Abdeljawad, F., Madison, J., Anderson, A. T., Fattebert, J.-L., Ferencz, R. M., Hodge, N. E., Khairallah, S. A., and Walton, O., 2017, "Modeling of additive manufacturing processes for metals: Challenges and opportunities," *Current Opinion in Solid State and Materials Science*, pp. Medium: ED; Size: p. 198-206. doi:
- [60] Denlinger, E. R., Irwin, J., and Michaleris, P., 2014, "Thermomechanical Modeling of Additive Manufacturing Large Parts," *Journal of Manufacturing Science and Engineering*, 136(6). doi: 10.1115/1.4028669

- [61] Lindgren, L.-E., Lundbäck, A., Fisk, M., Pederson, R., and Andersson, J., 2016, "Simulation of additive manufacturing using coupled constitutive and microstructure models," *Additive Manufacturing*, 12, pp. 144-158. doi: <https://doi.org/10.1016/j.addma.2016.05.005>
- [62] Dong, P., Song, S., and Zhang, J., 2014, "Analysis of residual stress relief mechanisms in post-weld heat treatment," *International Journal of Pressure Vessels and Piping*, 122, pp. 6-14. doi: <https://doi.org/10.1016/j.ijpvp.2014.06.002>
- [63] Matsumoto, M., Shiomi, M., Osakada, K., and Abe, F., 2002, "Finite element analysis of single layer forming on metallic powder bed in rapid prototyping by selective laser processing," *International Journal of Machine Tools and Manufacture*, 42(1), pp. 61-67. doi: [https://doi.org/10.1016/S0890-6955\(01\)00093-1](https://doi.org/10.1016/S0890-6955(01)00093-1)
- [64] Dunbar, A. J., Denlinger, E. R., Gouge, M. F., and Michaleris, P., 2016, "Experimental validation of finite element modeling for laser powder bed fusion deformation," *Additive Manufacturing*, 12, pp. 108-120. doi: <https://doi.org/10.1016/j.addma.2016.08.003>
- [65] Zhou, X., Zhang, H., Wang, G., and Bai, X., 2016, "Three-dimensional numerical simulation of arc and metal transport in arc welding based additive manufacturing," *International Journal of Heat and Mass Transfer*, 103, pp. 521-537. doi: <https://doi.org/10.1016/j.ijheatmasstransfer.2016.06.084>
- [66] Beeker, L. Y., Pringle, A. M., and Pearce, J. M., 2018, "Open-source parametric 3-D printed slot die system for thin film semiconductor processing," *Additive Manufacturing*, 20, pp. 90-100. doi: <https://doi.org/10.1016/j.addma.2017.12.004>
- [67] Yang, Q., Zhang, P., Cheng, L., Min, Z., Chyu, M., and To, A. C., 2016, "Finite element modeling and validation of thermomechanical behavior of Ti-6Al-4V in directed energy deposition additive manufacturing," *Additive Manufacturing*, 12, pp. 169-177. doi: <https://doi.org/10.1016/j.addma.2016.06.012>
- [68] Yang, Y., Allen, M., London, T., and Oancea, V., 2019, "Residual Strain Predictions for a Powder Bed Fusion Inconel 625 Single Cantilever Part," *Integrating Materials and Manufacturing Innovation*, 8(3), pp. 294-304. doi: 10.1007/s40192-019-00144-5
- [69] Wang, Z., Denlinger, E., Michaleris, P., Stoica, A. D., Ma, D., and Beese, A. M., 2017, "Residual stress mapping in Inconel 625 fabricated through additive manufacturing: Method for neutron diffraction measurements to validate thermomechanical model predictions," *Materials & Design*, 113, pp. 169-177. doi: <https://doi.org/10.1016/j.matdes.2016.10.003>
- [70] Mukherjee, T., Zhang, W., and DebRoy, T., 2017, "An improved prediction of residual stresses and distortion in additive manufacturing," *Computational Materials Science*, 126, pp. 360-372. doi: <https://doi.org/10.1016/j.commatsci.2016.10.003>
- [71] Xie, R., Chen, G., Zhao, Y., Zhang, S., Yan, W., Lin, X., and Shi, Q., 2019, "In-situ observation and numerical simulation on the transient strain and distortion prediction during additive manufacturing," *Journal of Manufacturing Processes*, 38, pp. 494-501. doi: <https://doi.org/10.1016/j.jmapro.2019.01.049>
- [72] Montevecchi, F., Venturini, G., Grossi, N., Scippa, A., and Campatelli, G., 2017, "Finite Element mesh coarsening for effective distortion prediction in Wire Arc Additive

- Manufacturing," Additive Manufacturing, 18, pp. 145-155. doi: <https://doi.org/10.1016/j.addma.2017.10.010>
- [73] Josupeit, S., Ordia, L., and Schmid, H.-J., 2016, "Modelling of temperatures and heat flow within laser sintered part cakes," Additive Manufacturing, 12, pp. 189-196. doi: <https://doi.org/10.1016/j.addma.2016.06.002>
- [74] Xie, R., Shi, Q., and Chen, G., 2020, "Improved distortion prediction in additive manufacturing using an experimental-based stress relaxation model," Journal of Materials Science & Technology, 59, pp. 83-91. doi: <https://doi.org/10.1016/j.jmst.2020.04.056>
- [75] Hodge, N. E., Ferencz, R. M., and Vignes, R. M., 2016, "Experimental comparison of residual stresses for a thermomechanical model for the simulation of selective laser melting," Additive Manufacturing, 12, pp. 159-168. doi: <https://doi.org/10.1016/j.addma.2016.05.011>
- [76] Afazov, S., Denmark, W. A. D., Lazaro Toralles, B., Holloway, A., and Yaghi, A., 2017, "Distortion prediction and compensation in selective laser melting," Additive Manufacturing, 17, pp. 15-22. doi: <https://doi.org/10.1016/j.addma.2017.07.005>
- [77] Martina, F., Mehnen, J., Williams, S. W., Colegrove, P., and Wang, F., 2012, "Investigation of the benefits of plasma deposition for the additive layer manufacture of Ti-6Al-4V," Journal of Materials Processing Technology, 212(6), pp. 1377-1386. doi: <https://doi.org/10.1016/j.jmatprotec.2012.02.002>
- [78] Marques, B. M., Andrade, C. M., Neto, D. M., Oliveira, M. C., Alves, J. L., and Menezes, L. F., 2020, "Numerical Analysis of Residual Stresses in Parts Produced by Selective Laser Melting Process," Procedia Manufacturing, 47, pp. 1170-1177. doi: <https://doi.org/10.1016/j.promfg.2020.04.167>
- [79] Desmaison, O., Pires, P.-A., Levesque, G., Peralta, A., Sundarraj, S., Makinde, A., Jagdale, V., and Megahed, M., "Influence of Computational Grid and Deposit Volume on Residual Stress and Distortion Prediction Accuracy for Additive Manufacturing Modeling," Springer International Publishing, pp. 365-374.
- [80] Peng, H., Ghasri-Khouzani, M., Gong, S., Attardo, R., Ostiguy, P., Gatrell, B. A., Budzinski, J., Tomonto, C., Neidig, J., Shankar, M. R., Billo, R., Go, D. B., and Hoelzle, D., 2018, "Fast prediction of thermal distortion in metal powder bed fusion additive manufacturing: Part 1, a thermal circuit network model," Additive Manufacturing, 22, pp. 852-868. doi: <https://doi.org/10.1016/j.addma.2018.05.023>
- [81] Ganeriwala, R., and Zohdi, T. I., 2016, "A coupled discrete element-finite difference model of selective laser sintering," Granular Matter, 18(2), p. 21. doi:
- [82] Chowdhury, S., and Anand, S., "Artificial Neural Network Based Geometric Compensation for Thermal Deformation in Additive Manufacturing Processes," Proc. ASME 2016 11th International Manufacturing Science and Engineering Conference V003T08A006.
- [83] Francis, J., and Bian, L., 2019, "Deep Learning for Distortion Prediction in Laser-Based Additive Manufacturing using Big Data," Manufacturing Letters, 20, pp. 10-14. doi: <https://doi.org/10.1016/j.mfglet.2019.02.001>

- [84] Escolano, F., Hancock, E. R., and Lozano, M. A., 2012, "Heat diffusion: Thermodynamic depth complexity of networks," *Physical Review E*, 85(3), p. 036206. doi: [10.1103/PhysRevE.85.036206](https://doi.org/10.1103/PhysRevE.85.036206)
- [85] Saito, N., 2013, "Tutorial: Laplacian Eigenfunctions - Foundations and Applications," University of California, Davis, Graduate University for Advanced Studies, National Institute of Fusion Science, Japan., doi:
- [86] Xiao, B., Hancock, E. R., and Wilson, R. C., 2009, "Graph characteristics from the heat kernel trace," *Pattern Recognition*, 42(11), pp. 2589-2606. doi: <https://doi.org/10.1016/j.patcog.2008.12.029>
- [87] Zhang, F., and Hancock, E. R., 2008, "Graph spectral image smoothing using the heat kernel," *Pattern Recognition*, 41(11), pp. 3328-3342. doi: <https://doi.org/10.1016/j.patcog.2008.05.007>
- [88] Peng, H., Go, D. B., Billo, R., Gong, S., Shankar, M. R., Gattrell, B. A., Budzinski, J., Ostiguy, P., Attardo, R., and Tomonto, C., "Part-scale model for fast prediction of thermal distortion in DMLS additive manufacturing; Part 2: a quasi-static thermo-mechanical model," *Proc. Solid Freeform Fabrication Symposium*, pp. 382-397.
- [89] Peng, H., Ghasri-Khouzani, M., Gong, S., Attardo, R., Ostiguy, P., Rogge, R. B., Gattrell, B. A., Budzinski, J., Tomonto, C., Neidig, J., Shankar, M. R., Billo, R., Go, D. B., and Hoelzle, D., 2018, "Fast prediction of thermal distortion in metal powder bed fusion additive manufacturing: Part 2, a quasi-static thermo-mechanical model," *Additive Manufacturing*, 22, pp. 869-882. doi: <https://doi.org/10.1016/j.addma.2018.05.001>
- [90] Yavari, R., Smoqi, Z., Riensche, A., Bevans, B., Kobir, H., Mendoza, H., Song, H., Cole, K., and Rao, P., 2021, "Part-scale thermal simulation of laser powder bed fusion using graph theory: Effect of thermal history on porosity, microstructure evolution, and recoater crash," *Materials & Design*, 204, p. 109685. doi: <https://doi.org/10.1016/j.matdes.2021.109685>
- [91] Stavropoulos, P., Foteinopoulos, P., Papacharalampopoulos, A., and Tsoukantas, G., 2019, "Warping in SLM additive manufacturing processes: estimation through thermo-mechanical analysis," *The International Journal of Advanced Manufacturing Technology*, 104(1), pp. 1571-1580. doi: [10.1007/s00170-019-04105-2](https://doi.org/10.1007/s00170-019-04105-2)
- [92] Mirkoohi, E., Dobbs, J. R., and Liang, S. Y., 2020, "Analytical mechanics modeling of in-process thermal stress distribution in metal additive manufacturing," *Journal of Manufacturing Processes*, 58, pp. 41-54. doi: <https://doi.org/10.1016/j.jmapro.2020.08.009>
- [93] Bugatti, M., and Semeraro, Q., 2018, "Limitations of the inherent strain method in simulating powder bed fusion processes," *Additive Manufacturing*, 23, pp. 329-346. doi: <https://doi.org/10.1016/j.addma.2018.05.041>
- [94] Cheng, B., and Chou, Y. K., "Thermal Simulations for Cooling Rate Mapping in Electron Beam Additive Manufacturing," *Proc. ASME 2015 International Mechanical Engineering Congress and Exposition*V02AT02A013.
- [95] Manshoori Yeganeh, A., Movahhedy, M. R., and Khodaygan, S., 2019, "An efficient scanning algorithm for improving accuracy based on minimising part warping in selected laser sintering process," *Virtual and Physical Prototyping*, 14(1), pp. 59-78. doi: [10.1080/17452759.2018.1511738](https://doi.org/10.1080/17452759.2018.1511738)

This work was funded by the **National Science Foundation** (NSF)

